Monthly Notices
of the
ROYAL ASTRONOMICAL SOCIETY

MNRAS **484,** 3356–3375 (2019)
Advance Access publication 2019 January 24

doi:10.1093/mnras/stz227

# The Milky Way like galaxy NGC 6384 and its nuclear star cluster at high NIR spatial resolution using LBT/ARGOS commissioning data

Iskren Y. Georgiev,[1★] Nadine Neumayer,[1] Wolfgang Gässler,[1] Sebastian Rabien,[2] Lorenzo Busoni,[3] Marco Bonaglia,[3] Julian Ziegleder,[2] Gilles Orban de Xivry,[4] Diethard Peter,[1] Martin Kulas,[1] Jose Borelli,[1] Gustavo Rahmer,[5] Michael Lefebvre[5] and Holger Baumgardt[6]

[1]*Max-Planck Institut für Astronomie, Königstuhl 17, D-69117 Heidelberg, Germany*
[2]*Max-Planck Institut für Extraterrestrische Physik, Giessenbachstrasse 1, D-85748 Garching, Germany*
[3]*Arcetri Astrophysical Observatory, Largo Enrico Fermi 5, I-50125 Florence, Italy*
[4]*Université de Liège, Institut d'Astrophysique et de Géophysique (Bât. B5c), Quartier Agora, Allée du 6 août, 19C, B-4000 Liège 1 (Sart-Tilman), Belgium*
[5]*LBT Observatory, University of Arizona, 933 N. Cherry Ave, Tucson, AZ 85721, USA*
[6]*University of Queensland, St. Lucia, Brisbane, QLD 4068, Australia*

Accepted 2019 January 18. Received 2019 January 17; in original form 2018 October 26

## ABSTRACT

We analyse high spatial resolution near infrared (NIR) imaging of NGC 6384, a Milky Way like galaxy, using ARGOS commissioning data at the Large Binocular Telescope (LBT). ARGOS provides a stable $\mathrm{PSF_{FWHM}} = 0\farcs2$–$0\farcs3$ AO correction of the ground layer across the LUCI 2 NIR camera 4 × 4 arcmin field by using six laser guide stars (three per telescope) and a natural guide star for tip-tilt sensing and guiding. Enabled by this high spatial resolution, we analyse the structure of the nuclear star cluster (NSC) and the central kiloparsec of NGC 6384. We find via 2D modelling that the NSC ($r_{\rm eff} \simeq 10$ pc) is surrounded by a small ($r_{\rm eff} \simeq 100$ pc) and a larger Sersić ($r_{\rm eff} \simeq 400$ pc), all embedded within the NGC 6384 large-scale boxy/X-shaped bulge and disc. This proof-of-concept study shows that with the high spatial resolution achieved by ground-layer AO we can push such analysis to distances previously only accessible from space. SED-fitting to the NIR and optical *HST* photometry allowed to leverage the age–metallicity–extinction degeneracies and derive the effective NSC properties of an young to old population mass ratio of 8 per cent with $\mathcal{M}_{\star,\rm old} \simeq 3.5 \times 10^7\,\mathrm{M_\odot}$, $\mathrm{Age_{old,\,young}} = 10.9 \pm 1.3$ Gyr and 226 Myr ±62 per cent, metallicity $[M/H] = -0.11 \pm 0.16$, and $0.33 \pm 39$ per cent dex, and $E(B-V) = 0.63$ and 1.44 mag.

**Key words:** galaxies: nuclei; galaxies: individual: NGC6384.

## 1 INTRODUCTION

The development of current telescope technology is *essential* to increase the efficiency of scientific output. In particular, high spatial resolution over a large field of view is one such domain that was recently commissioned at the Large Binocular Telescope (LBT;[1] Hill 1994; Hill et al. 2012) on Mount Graham in Arizona. The Advanced Rayleigh guided Ground layer adaptive Optics System, (ARGOS[2]; Rabien et al. 2018), equips the LBT with six green light (532 nm) lasers [three on each side situated on a circle with 2 arcmin radius (see Fig. 1)]. ARGOS corrects the ground layer turbulence by using artificial laser stars focused at 12 km and a tip-tilt star for wave front sensing and guiding. This improves the near infrared (NIR) natural seeing by a factor of 2–3, and provides a stable point spread function (PSF) over a 4 × 4 arcmin field of view with $\lesssim$20 per cent increase towards the detector edges. Together with the NIR cameras LUCI 1 & 2 (see Section 2) this makes LBT uniquely equipped for high spatial resolution NIR science. A dedicated ARGOS paper describing its technical aspects, performance, and commissioning results is published by Rabien et al. (2018). The aim of this paper is to utilize the large field of view AO correction and push the limits to study the structure of compact star clusters beyond distances accessible for ground based seeing limited observations.

Here we focus on the spatial analysis of the nuclear star cluster (NSC) and its host galaxy NGC 6384 at a distance of 20.7 Mpc ($m - M = 31.58$ mag; Sorce et al. 2014). In a forthcoming paper we will present the analysis of the star cluster population of NGC 6384. This galaxy was selected as a first scientific commissioning target due to the large amount of Galactic stars suitable for performance testing. In addition, its stellar mass ($\sim 5 \times 10^{10}\,\mathrm{M_\odot}$; Georgiev

★ E-mail: georgiev@mpia.de; iskren.y.g@gmail.com
[1]http://www.lbto.org/
[2]http://www.mpe.mpg.de/ir/argos

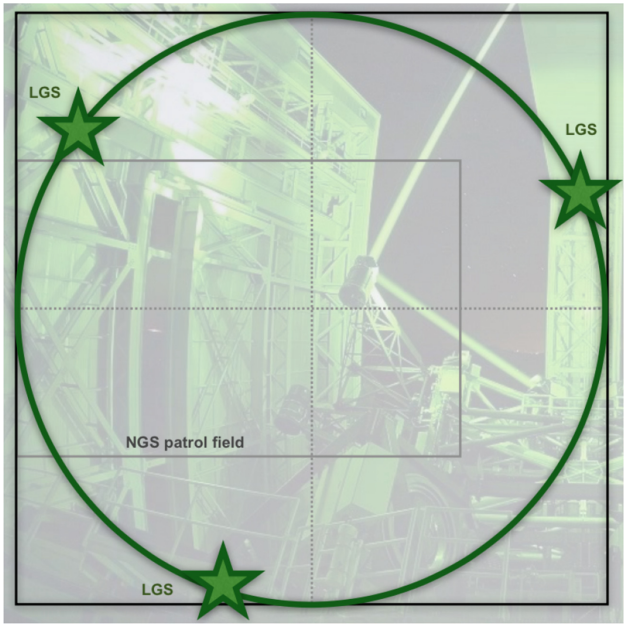


**Figure 1.** Schematic view of the 4 × 4 arcmin LUCI 2 field of view (solid, black outer square), the ∼3 × 2 arcmin field of the NGS camera board (light, grey rectangle), and the 2 arcmin radius circle (thick, green line circle), where the three LGSs are located within the LUCI FoV.

et al. 2016) and boxy/peanut bulge structure (Erwin & Debattista 2013) make it appear very similar to the Milky Way (MW). Its NSC is more extended but of comparable mass ($r_{\rm eff,\,V} \sim 15$ pc, $\mathcal{M} \simeq 1.3 \times 10^7\,{\rm M}_\odot$, Georgiev & Böker 2014; Georgiev et al. 2016, and found here in the NIR) to that of the MW nuclear cluster ($r_{\rm eff,K_S} = 4.2$ pc, $\mathcal{M} = 2.5 \times 10^7\,{\rm M}_\odot$, Schödel et al. 2014). The similar mass might suggest that it is possible to host a similarly massive black hole (MBH) of $4.1 \times 10^6\,{\rm M}_\odot$ (Feldmeier-Krause et al. 2017; Gravity Collaboration 2018). A potential MBH would also explain its classification as a LINER galaxy (Ho, Filippenko & Sargent 1997). This makes it a good test case in studying the NSC NIR properties of a MW analogue at ∼ 21 Mpc. The main difference to the MW, however, is its very low galaxy density environment. To within $\pm 400\,{\rm km\,s^{-1}}$ of its systemic velocity ($1664\,{\rm km\,s^{-1}}$)[3] the nearest bright galaxy is NGC 6509 ($1813\,{\rm km\,s^{-1}}$, ∼2.5 mag fainter than NGC 6384) at a projected separation of ∼2.5 Mpc (∼6.7°) and is also twice less massive (∼$2 \times 10^{10}\,{\rm M}_\odot$; Georgiev et al. 2016).

Due to the high-density nature of NSCs (compact ∼4 pc and massive, ∼$10^6\,{\rm M}_\odot$, e.g. Böker et al. 2002, 2004; Walcher et al. 2005; Georgiev & Böker 2014; Georgiev et al. 2016; Ordenes-Briceño et al. 2018; Sánchez-Janssen et al. 2018), obtaining high spatial resolution data in the NIR is crucial to break the age–metallicity–reddening degeneracies present in the optical alone (e.g. de Meulenaer et al. 2014). This is very important for studying their properties, where young stellar populations and high extinction are expected to be present. Spatially resolving these provides important constraints on our understanding of how galactic nuclei and NSCs build-up, e.g. via cluster migration and merging (e.g. Tremaine, Ostriker & Spitzer 1975; Capuzzo-Dolcetta 1993; Oh & Lin 2000; Bekki et al. 2004; Antonini et al. 2012; Tsatsi et al. 2017) or *in situ* from gas accretion (e.g. Böker, Lisenfeld & Schinnerer 2003; Schinnerer, Böker & Meier 2003; Milosavljević 2004; Schinnerer et al. 2006; Bekki 2007) or most likely a combination of both (e.g. Hartmann et al. 2011; Neumayer et al. 2011; Antonini, Barausse & Silk 2015; Cole et al. 2017; Kacharov et al. 2018). In addition, studies of NSCs have shown that their size increases with wavelength (Georgiev & Böker 2014; Carson et al. 2015), which is consistent with earlier findings that NSCs contain morphologically distinct young and old stellar populations (Seth et al. 2008), where the young one is more centrally concentrated. From numerical simulations it is known that due to energy equipartition and orbital relaxation merging of clusters typically leads to a final cluster with larger effective radius ($r_{\rm eff}$) (e.g. Fellhauer & Kroupa 2002; Bekki et al. 2004). On the other hand NSC growth dominated by episodic gas accretion will lead to a more compact cluster (e.g. Tsang & Milosavljević 2018).

Optical-NIR Spectral Energy Distribution (SED) modelling of diffuse light (e.g. Carson et al. 2015; Dale et al. 2016) at high spatial resolution can provide a map of the spatial variation and composition of the main stellar population components of the NSC, as well as their host galaxy. Such analysis can also unveil (an additional) contribution to the optical-NIR light from accretion on to an obscured nuclear MBH and/or nuclear star formation activity (e.g. Noll et al. 2009; Drouart et al. 2016). To understand NSC formation, it is therefore critical to be able to disentangle such degeneracies. For example, follow-up spectroscopic observations aiming at decomposing the main stellar populations and the dynamical imprint of a MBH rely on a good mass model to predict the stellar population velocity profile (e.g. Häring-Neumayer et al. 2006; Seth et al. 2010; Neumayer et al. 2011; Neumayer & Walcher 2012; Nguyen et al. 2018). Observations of NSCs have shown that although they contain young stellar populations and extended star formation histories (SFHs), the most dominant one by mass is the oldest ($\gtrsim$3 Gyr), where more than 50 per cent of the mass of the cluster has formed (e.g. Walcher et al. 2006; Kacharov et al. 2018, from spectral modelling in the optical). Therefore, characterizing the spatial structure of NSCs in the NIR is of particular importance, because that is where most of the stellar light of the old stellar population is emitted that allows us to trace most of the gravitating mass. Therefore, characterizing NSCs in the NIR can provide additional constraints as to which of the leading NSC formation scenarios had a major role in the formation of particular NSC. However, to be able to achieve this for a larger sample and of more distant galaxies, efficient high spatial resolution observations are required, such as with the presented here wide-field ground-layer AO NIR observations in the NIR with ARGOS at the LBT.

Here we first present the observations, data reduction, and calibrations in Section 2. In Section 3, we present our analysis of the data with the colour−magnitude diagram (CMD, in Section 3.1) of all sources in the LUCI 2 field of view of NGC 6384 and in Section 3.2 we present the structural analysis of the NSC and NGC 6384. In Section 3.3, we combine the optical photometry from archival *HST* data and the LUCI 2 NIR photometry to derive via SED fitting the NSC effective age, luminosity-weighted mass, metallicity, and reddening. Finally, in Section 4, we discuss and summarize our findings.

## 2 OBSERVATIONS, REDUCTION, AND CALIBRATION

### 2.1 Near infrared LBT/LUCI 2 data and PSF photometry

NGC 6384 imaging data were obtained during the ARGOS commissioning run on 2015-05-01 and 02. The total integration time in closed loop with the LBT/LUCI 2 NIR camera (Seifert et al. 2003)

[3] Velocity information has been retrieved from the HyperLeda data base (Makarov et al. 2014).

**Figure 2.** $JHK_S$ colour composite image of a $2\farcm5 \times 2\farcm5$ ($\sim$18 $\times$ 18 kpc) region of NGC 6384 taken with the LUCI 2 camera on LBT during the first ARGOS commissioning run in 2015-05-02. The achieved spatial resolution across the LUCI 2 4 $\times$ 4 arcmin field is $\sim 0.25'' \pm 20$ per cent. The intensity scale is stretched such that to show the compact nucleus, the bar and X-shaped boxy bulge, and spiral arms of NGC 6384. North is up, and East is to the left.

and a detector integration time (DIT) = 5 s is $J(775s)$, $H(860s)$, $K_S$ (70$s$), i.e. 155, 172, and 14 frames per filter, respectively. Due to constraints from commissioning tasks, the $K_S$-band data were not fully completed. Nevertheless, as we will show later (Section 3.1), the depth was sufficient enough for our analysis of the NSC and the brightest GCs. The latter will be investigated in a forthcoming study, while here we focus our analysis only on the NSC and the central kiloparsec of NGC 6384. A colour composite $JHK_S$ image of NGC 6384 shown in Fig. 2 is zoomed at the central $\sim$3 $\times$ 3. The intensity scaling is adjusted such that it better shows various galactic structures (nucleus, bar, bulge, spiral arms). The brightest star (middle-bottom) is the used as the tip-tilt star (a Natural Guide Star, NGS, for Wave Front Sensing, WFS). The LUCI 2 plate scale of $0\farcs1189\,\mathrm{pix}^{-1}$ corresponds to $12\,\mathrm{pc\,pixel}^{-1}$ at the distance to NGC 6384 of 20.7 Mpc. We used a rectangular dither pattern within $\sim$12 arcsec to eliminate detector cosmetics (bad pixels). The dither pattern is also chosen such that the NGS stays within the field of view of the NGS camera board, shown with grey solid rectangle in Fig. 1. In this schematic representation one can see that the ARGOS LGSs are situated on a circle with a radius of 2 arcmin, where their exact location depends on the field orientation. Off-target sky frames beyond the galaxy extent were unfortunately not obtained due to technical limitations during this first science commissioning run. Nevertheless, we are able to obtain a good global photometric calibration by using about 30 stars in common with the 2 MASS point source catalogue (details follow below).

Image reduction was performed with tasks in IRAF.[4] We first correct all data frames for pixel non-linearity and persistence (see Section A). Although LUCI 2 is cryogenically cooled, we create a master dark frame to account for the low level thermal dark current. Flats taken at the end of the observation were used to obtain a normalized master flat to correct for pixel-to-pixel differences in quantum efficiency, illumination, and sensitivity across the detector. We create a bad pixel map from the ratio between low- and high-count flats. From each science exposure we subtracted the master dark and divided by the normalized flat. The final image registration and coaddition were performed in identical manner as in Georgiev et al. (2008), Georgiev, Goudfrooij & Puzia (2012), and Georgiev & Böker (2014) with a self-developed IRAF procedure.[5] It matches stars across all exposures, computes geometric distortions, uses the bad pixel map to flag pixels and a 15 $\times$ 15 pixel image statistic region to compute zero level offsets with respect to a reference exposure. Using pixel statistic region guarantees minimum biases and introduction of noise to objects' fluxes due to eventual residuals from imperfect background sky subtraction. This way we obtained the final coadded images in each band. We note that the same physical location of the statistic region was adopted for all filters. This is important in order to minimize biases in the final photometric colours.

Thanks to the ARGOS ground layer atmospheric correction, our final combined images achieved an excellent resolution of $\mathrm{PSF_{FWHM}} \simeq 0\farcs2$ from the central tip tilt star to $\leq 0\farcs3$ at the detector borders (see details in Section B). To properly account for the variable PSF across the detector, we used the large number of Galactic foreground stars (>100) to build a spatially variable PSF model in each filter. The model[6] is used to perform a PSF photometry on all detections above $\geq 2 \times \sigma_{\mathrm{bckgr}}$ threshold with a PSF model radius of 9 pix $\simeq$ 1 arcsec $\simeq 4 \times \mathrm{PSF_{FWHM}}$. The aperture correction is derived from curve of growth aperture photometry of the PSF stars.

The photometric zero-points are obtained from the error weighted least-squares fit through the difference between the 2MASS and instrumental magnitude against 2MASS magnitude and colour that yield the photometric zero-points in $J$, $H$, and $K_S$ of $25.891 \pm 0.013$, $25.654 \pm 0.013$, and $24.922 \pm 0.023$ mag, respectively. We also checked for $J - K_S$ colour dependence, and found it to be negligible compared to the photometric uncertainties, which is driven by the faintest stars with worst 2MASS photometry and most affected by the background noise. Finally, the magnitudes are corrected for foreground Galactic reddening $A_J, A_H$ , and $A_{Ks} = 0.087, 0.055$, and 0.037 mag based on $E(B - V) = 0.11$ mag from the Schlafly & Finkbeiner (2011)'s recalibration of the Schlegel, Finkbeiner & Davis (1998) Galactic dust maps and assuming Fitzpatrick (1999) reddening law with $R_V = 3.1$.

### 2.2 Optical *HST* data reduction and PSF model

We retrieved from the *HST* archive WFPC 2 ($F606W$) and ACS/WFC ($F475W$, $F814W$) data from Cycle 6 and 11 programs SNAP-6359 (PI: M. Stiavelli) and GO-9395 (PI: M. Carollo), respectively. We used the latest version of the ASTRODRIZZLE routine

[4]IRAF is the image reduction and analysis facility, a general purpose software system for the reduction and analysis of astronomical data. IRAF is written and supported by the National Optical Astronomy Observatories (NOAO) in Tucson, Arizona. NOAO is operated by the Association of Universities for Research in Astronomy (AURA), Inc. under cooperative agreement with the National Science Foundation

[5]A wrapper routine for the IRAF procedures DAOFIND, DAOPHOT, ALLSTAR, GEOMAP, GEOTRAN, and IMCOMBINE.

[6]The empirical PSF was best fit by a single Moffat function, unlike the complex PSF of full AO systems.

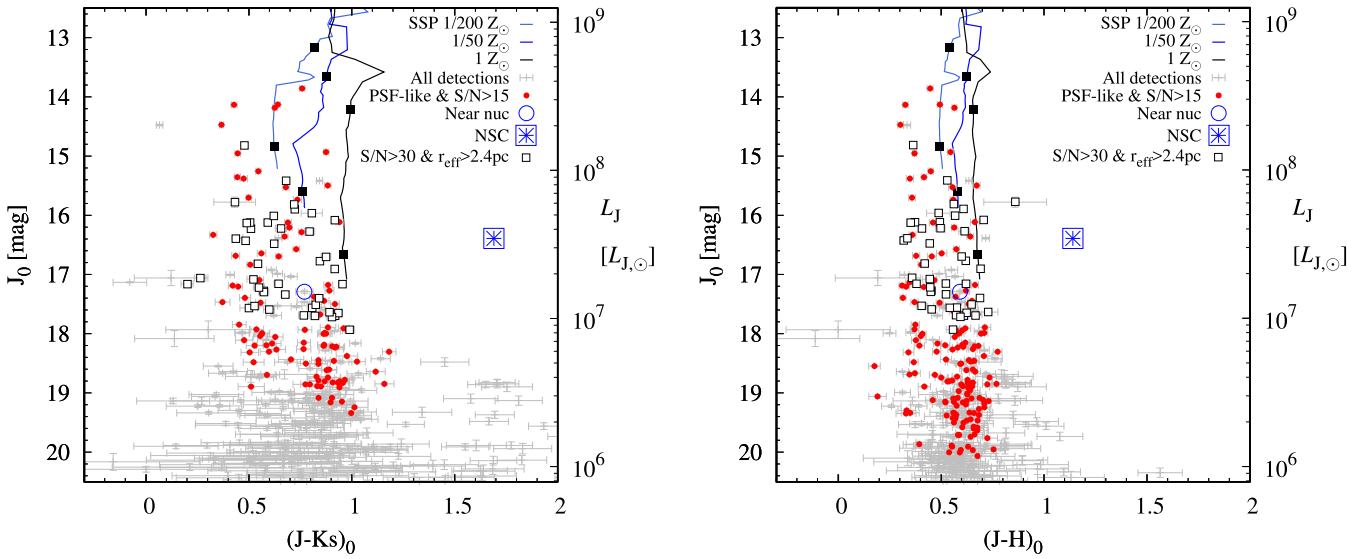


**Figure 3.** Foreground Galactic deredenned CMDs $J_0$ versus $(J - K_S)_0$ (**left**) and versus $(J - H)_0$ (**right**) of sources in the 4 × 4 arcmin LUCI 2 field of NGC 6384. Grey symbols with errorbars are all detections. Filled (red) circles are S/N > 15 sources with a stellar-like PSF. Open squares are sources with S/N > 30 for which the additional PSF analysis suggests a size bigger than 10 per cent of the $PSF_{FWHM}$, i.e. >2.4 pc at the distance of NGC 6384. The large open (blue) circle is a bright near nuclear source suspected to be a massive star cluster projected close to the NSC. Asterisk indicates the integrated NSC magnitude and colour. For comparison, with solid (nearly vertical) lines we show scaled Bruzual & Charlot (2003) SSP models with metallicity of a solar, 1/50 ([*Z*/*H*] = −0.7 dex) and 1/200 ([*Z*/*H*] = −2.3 dex), as indicated in the figure legend. Two solid (black) squares along each SSP track indicate an age of 2 and 14 Gyr from top to bottom, respectively. The model tracks are scaled such that the most metal-poor track at 14Gyr has roughly $10^8 L_{J_\odot}$.

in PYRAF[7] to re-process the archival data in order to achieve optimal drizzling pixel fraction and final pixel scale. Since the central ∼5 × 5 kpc of NGC 6384 are fully covered by the higher resolution WFPC PC chip (0.05 arcsec pixel$^{-1}$), we restricted our analysis to only this WFPC 2 detector. Its resolution is nearly identical to that of the ACS WFC (0.04 arcsec pixel$^{-1}$), therefore we chose to drizzle the WFPC2/PC1 and the ACS images to the same final pixel scale of 0.05 arcsec pixel$^{-1}$. We did not go for a smaller pixel scale due to the limited number of only two single exposures. We found that the optimal drizzle pixel fraction to be 0.85. Due to the large extent of the galaxy, we did not allow ASTRODRIZZLE to automatically derive the sky value, instead, we provided our own. This value was obtained from the outermost galaxy sections on the ACS detectors. We obtained camera, detector, filter, and position specific PSF model with the TINYTIM software package (Krist, Hook & Stoehr 2011), which we drizzled with the identical ASTRODRIZZLE set up for the science images. Similarly to Section 2.1, the filter specific Galactic reddening towards NGC 6384 is $A_{F435W} = 0.434$ mag, $A_{F606W} = 0.293$ mag, and $A_{F814W} = 0.180$ mag.

## 3 ANALYSIS

In this section, we present the derived photometric properties of all sources in the LUCI 2 field of NGC 6384, including candidate star clusters whose detailed analysis we will present in a forthcoming study. We derive the structure of the NSC by fitting simultaneously its surroundings (10 × 10 kpc). We also analyse in identical manner the archival *HST*/ACS images. Using SED fitting of the NIR-optical best-fitting model magnitudes we derive luminosity weighted integrated properties of the NSC (e.g. stellar populations mass, age, metallicity, etc.). Similarly, we also compute a 1D projected of the surface mass density, metallicity, stellar population composition (young and old).

### 3.1 Colour–magnitude diagram of the NGC 6384 field

First, to illustrate the importance of the $K_S$ band in stellar population analysis in Fig. 3 left and right we compare $J - K_S$ and $J - H$ CMDs, respectively, of all three filter matched sources with PSF photometry. Due to technical and time limitations during the ARGOS commissioning run, the $K_S$- band data did not reach as deep as in the *J* and *H* bands. Although shallower, the $J - K_S$ colour index is scientifically more informative for the metallicity distribution of the sources, because it is largely sensitive to the stellar effective temperature, which in turn is sensitive to metallicity. This can be appreciated by the comparison with single stellar population (SSP) model tracks from Bruzual & Charlot (2003) shown with lines in Fig. 3 for three metallicities indicated in the figure legend. Evidently, the dynamical range in the $J - K_S$ colour and separation between the SSP models of different metallicity is significantly larger than the colour uncertainty, which is important for estimating photometric metallicity.

Secondly, to demonstrate the achieved high spatial resolution over the entire 4 × 4 arcmin field with filled (red) circles we show sources with S/N > 15 and stellar PSF, i.e. their sharp value[8] is within |sharp| = 0.15. Open squares indicate sources with S/N ≥ 30 and effective radius $r_{\rm eff} \geq 2.4$ pc as measured with the ISHAPE

[7] PYRAF is a product of the Space Telescope Science Institute, which is operated by AURA for NASA. PYRAF is PYTHON environment for running IRAF tasks

[8] The sharp value is roughly the difference between object and stellar PSF returned by ALLSTAR during the PSF photometry. Values close to 0 are stars, large positive bulges of background unresolved galaxies, and negative values are bad/hot pixels or cosmic rays.

code (Larsen 1999). For high S/N ≥ 30 sources Larsen (1999) has shown that reliable size measurements can be performed down to ∼10 per cent of the $PSF_{FWHM}$. In our case this spatial 'resolution' limit corresponds to $r_{eff} \geq 2.4$ pc at the distance to NGC 6384. The size measurement with ISHAPE was performed analogous to Georgiev et al. (2008) and Georgiev & Böker (2014). In brief, ISHAPE performs a $\chi^2$ minimization fitting of the object's profile with an analytical function convolved with a PSF model tailored to the objects' position on the detector (cf. Section 2.2). We fitted King (1962) profiles with fixed and variable concentration index parameter $r_t/r_c = C = 5, 15, 30, 100$. The model with the best $\chi^2$ fit was adopted to be the model for the object's structural parameters. The analysis of the extended objects (some likely GC candidates) will be presented in a forthcoming study since our aim here is to focus on the NSC and NGC 6384's large-scale analysis. With large open circle we indicate a bright near nuclear source, which we investigate later whether it could be a star cluster or a foreground star.

The integrated magnitude and colour of the NSC is shown with asterisk in Fig. 3 (details on the NSC photometry in Section 3.2). Before we model the NSC SED in Section 3.3, here we perform a qualitative assessment of the expected NSC mass based on its luminosity. The NSC has a *J*-band luminosity of $\sim 4 \times 10^7 L_{J,\odot}$ (cf. Fig. 3), which will correspond to a mass of $\sim 2 \times 10^7$ $M_\odot$, for a $M/L_J \sim 0.4$ increasing by ∼0.1 from low to high metallicity estimated from Bruzual & Charlot (2003) SSP models for an old ($t \simeq 5$ Gyr) stellar population. For a 14 Gyr old SSP, the *M*/*L* is roughly 0.9, i.e. it would be a factor of two more massive. For comparison, the Galactic NSC has a mass of the same order ($2.4 \times 10^7$ $M_\odot$, Schödel et al. 2007, 2014; Feldmeier et al. 2014). We also note that the NSC of NGC 6384 shows a fairly red $J - K_S$ colour compared to the rest of the sources and the SSP tracks in the CMD. Such a colour is, however, typical for a galactic nuclear source, which can be composed by a mixture of old and young stellar populations and more importantly, could be highly reddened. Therefore, to lift various degeneracies in Section 3.3 we combine our NIR with the *HST* optical data to perform a detailed SED analysis of the NSC stellar population composition and reddening.

### 3.2 Structure and photometry of the NSC and NGC 6384

As it can be seen in Fig. 2, NGC 6384 has a boxy bulge. An indication for an X-shape is better seen in the residual $K_S$-band image in Fig. 5(b), which is similar to that of the MW (e.g. Dwek et al. 1995; McWilliam & Zoccali 2010; Ness & Lang 2016; Abbott et al. 2017) and M 31 (Athanassoula & Beaton 2006; Beaton et al. 2007), as well as in many other galaxies (e.g. Laurikainen et al. 2011; Erwin & Debattista 2017). The boxy bulge was also quantified from seeing limited WHT/INGRID $K_S$-band data by Erwin & Debattista (2013), who expectedly were unable to resolve the nuclear cluster. Georgiev & Böker (2014) analysed the *HST*/WFPC 2 *F606W* image of the NSC and fitted its profile with a single King (King 1962) model using ISHAPE and obtained a half-light radius of $r_{eff} = 15.9^{+0.5}_{-0.0}$ pc. Here we re-analyse that data too to account for the other structures that might bias the $r_{eff}$, especially in the inner 1–2 arcsec. In particular, we focus on the central 3.6 × 3.6 kpc (∼36 × 36 arcsec) region of NGC 6384, which covers the bar, the boxy bulge and parts of the galaxy disc (Fig. 4 top). We focus only on this area, because it is sufficient for the analysis of the NSC and it is fully covered by the archival *HST*/WFPC 2 high-resolution (0.05 arcsec pixel$^{-1}$) PC 1 chip, and the ACS camera drizzled to identical resolution (see Section 2.2). For all images,

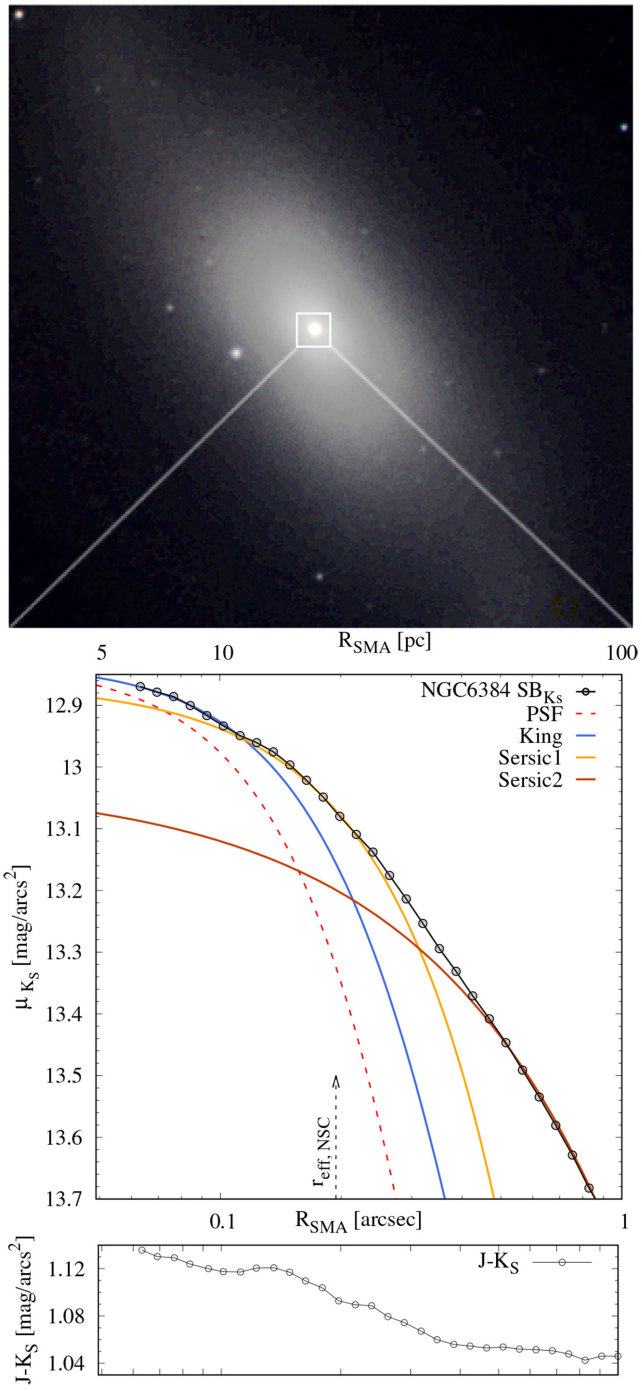


**Figure 4.** **Top:** $JHK_S$ image of NGC 6384 central 3.6 × 3.6 kpc (∼36 × 36 arcsec). **Middle:** $K_S$ surface brightness profile (line with circles) of the nuclear $r = 1$ arcsec (100 pc). Various components obtained from 2D fitting (see figure legend) illustrate the resolved nature of the NSC. **Bottom:** $J - K_S$ surface colour profile.

we first perform a simple isophotal fitting with the ELLIPSE task in IRAF/PYRAF, which gives a good idea for various sub-structures (e.g. dust lanes) when we subtract the fitted isophotal model from the image. We note that the ELLIPSE task does not account for the PSF during the SB extraction, therefore, the magnitude and colour SB-profiles shown here are merely for illustration purposes and should not be considered for quantitative analysis by the reader for

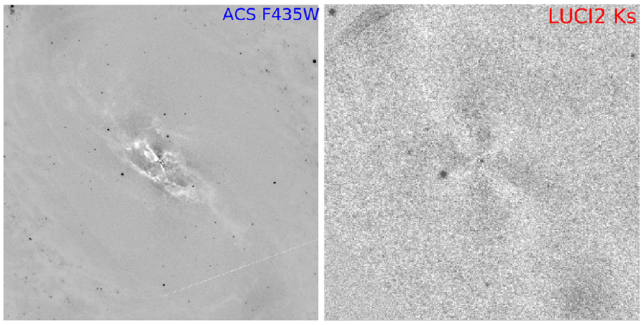


**Figure 5.** Residual images from the subtraction of an elliptical model. The dusty disc/lane seen in the optical/blue *F*435*W* band (left) is, expectedly, completely transparent in the NIR $K_S$ filter. Pixel masks for all filters were constructed from these residual images and are used for multicomponent 2D modelling. Both panels have identical size of 3.6 × 3.6 kpc (36 × 36 arcsec).

radii smaller or comparable to the PSF radius ($r \lesssim 0.12$ arcsec). We show an example of the residual images from subtracting the ELLIPSE model in Fig. 5, for the two filters more and less affected by extinction: the ACS/*F*435*W* (B) and the LUCI 2 $K_S$, respectively. It is evident that there is a prominent dusty disc/lane swirling around the nuclear zone (2.5 × 5 arcsec ≃ 250 × 500 pc), which expectedly is completely transparent in the NIR $K_S$ band. From these images for all filters we create a pixel mask, which we use in a next iteration with ELLIPSE and later on during the 2D fitting. In Fig. 4 (middle) we present the $K_S$ band 1D surface brightness (SB) profile (line connected open circles), because it is least affected by extinction, has the sharpest PSF of our NIR data and traces the old stellar population that dominates the mass. In the figure we only show the inner $r = 1$ arcsec (∼100 pc) to illustrate the high spatial resolution achieved with ARGOS and the resolved nature of the NSC. Clearly, the NSC is well resolved beyond the PSF (dashed, red line in Fig. 4) and it is well represented by a King profile (solid, blue curve), whose parameters we derived as explained below. A second component immediately surrounding the NSC is also clearly seen at $r \sim 0.2$ arcsec ≃ 15 pc, which is featured by a small bump in $J - K_S$ colour shown in the bottom panel of Fig. 4. This feature is less prominent in the SB-profile from the *HST*/ACS *F*814*W* image shown in Fig. 6, which is likely pointing to the fact that it is an old structure or/and more obscured in the optical. However, we see that a different component is becoming more prominent starting at around ∼0.3 arcsec, which suggests that it must be composed of younger stellar population. To avoid over interpretation of the colour profiles shown in Figs 4 and 6 we note at this point that due to the fact that ELLIPSE does not account for the PSF, the apparent marginal trend of redder colour (if any) in the core $r \lesssim 0.12$ arcsec are mainly due to the sharper PSF in the redder filter. We further discuss these components and colour trends in Section 4. The point is that in order to extract correctly the properties of the NSC, we need to simultaneously fit for all these components in 2D and on larger scale in all filters with their respective PSFs.

We model the light profile of the central 3.6 × 3.6 kpc (∼36 × 36 arcsec) of NGC 6384 and its NSC with IMFIT[9] (Erwin 2015). This software package performs a 2D profile fitting using the image PSF, a large choice of analytical profiles, iterative fitting minimization techniques ($\chi^2$, maximum-likelihood), bootstrapping, and MCMC modules for exploring and deriving more reliable values of the fitted

[9]http://www.mpe.mpg.de/∼erwin/code/imfit/

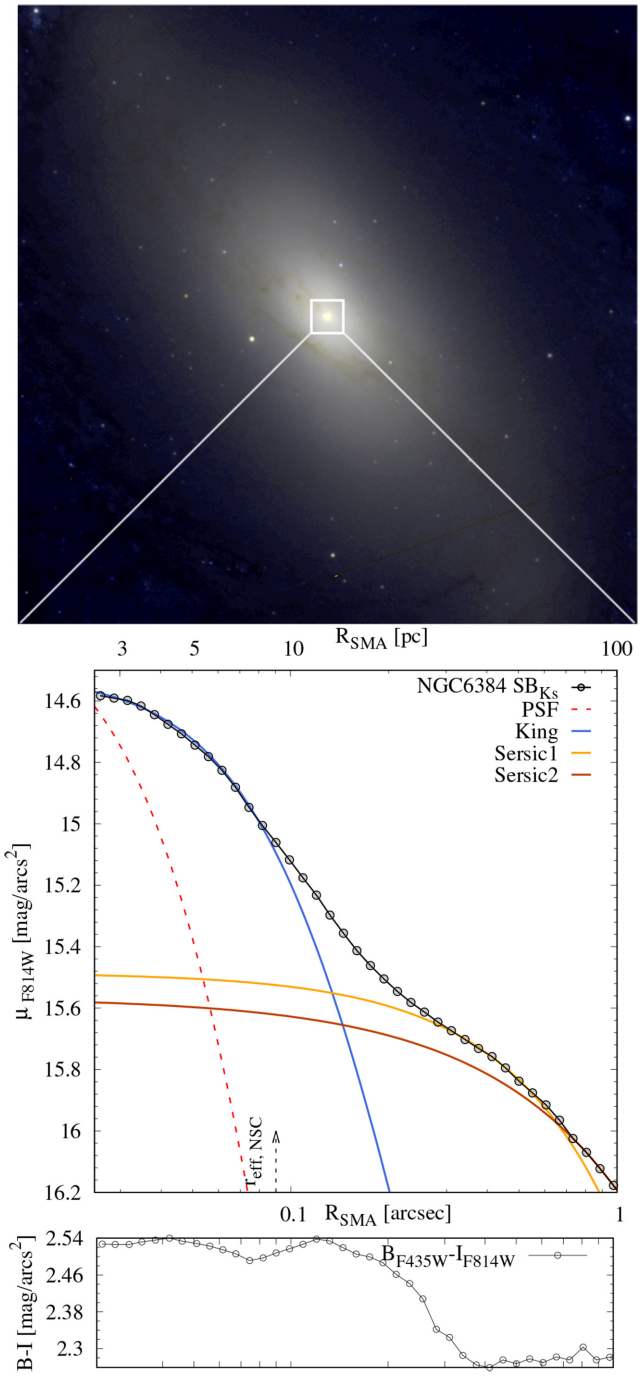


**Figure 6. Top:** Two filter (*F*435*W*, *F*814*W*) *HST*/ACS colour composite image of NGC 6384 of the same area as in Figs 4 and 8. Contrast and scaling are adjusted to clearly see the NSC and the dusty disc-like feature. **Middle:** *I*-band (*F*814*W*) SB. **Bottom:** $B - I$ colour profiles of the indicated area. Magnitudes are corrected for foreground Galactic reddening only.

parameters and their uncertainties. The high S/N of the NSC, allows us to use a 10× oversampled PSF to fit the central 10 × 10 pixels (∼1.2 arcsec ≃ 120 pc). We experimented with a wide range of analytical models available in IMFIT and found that a five-component model described best the fitted area (see Table 1). Namely, the NSC at the very centre was best fit by a modified King (1962) model with concentration, core radius, and $\alpha$ as fitted parameters (Elson 1999; Peng et al. 2010). The inner $r \lesssim 2$ arcsec ≃ 200 pc

**Table 1.** Best-fitting parameters for the NSC and the inner 1 kpc of NGC 6384. Each table block gives the parameter values of the respective fitted profile type.

| Profile (1) | $B_{F435W}$ (2) | $V_{F606W}$ (3) | $I_{F814W}$ (4) | $J$ (5) | $H$ (6) | $K_S$ (7) |
|---|---|---|---|---|---|---|
| King (the NSC) | | | | | | |
| Mag[a] | 21.61 | 19.98 | 18.56 | 16.39 | 15.25 | 14.70 |
| $r_{\rm eff}$ (pc)[b] | 5.8 | 10.1 | 9.1 | 13.9 | 11.8 | 19.5 |
| $r_c$ (pc) | $0.71^{+0.5}_{-0.3}$ | $1.59^{+0.4}_{-0.4}$ | $1.94^{+0.01}_{-0.4}$ | $2.87^{+0.10}_{-0.10}$ | $2.32^{+1.1}_{-0.4}$ | $4.26^{+0.09}_{-1.0}$ |
| $C$ | $146.6^{+3.1}_{-0.2}$ | $155.02^{+0.7}_{-21.7}$ | $86.4^{+8.5}_{1.6}$ | $97.27^{+3.6}_{-2.9}$ | $87.5^{+13.04}_{3.1}$ | $74.0^{+7.1}_{-6.8}$ |
| $\alpha$ | $1.28^{+0.28}_{-0.28}$ | $1.98^{+0.40}_{-0.40}$ | $2.08^{+0.58}_{-0.18}$ | $2.13^{+0.08}_{-0.10}$ | $1.86^{+0.21}_{-0.10}$ | $1.94^{+0.98}_{-1.08}$ |
| Sersić (disc/bulge?) | | | | | | |
| Mag | 17.30 | 16.00 | 15.35 | 14.21 | 13.59 | 13.22 |
| $n$ | $0.78^{+0.01}_{-0.01}$ | $0.76^{+0.01}_{-0.01}$ | 0.79 | 0.724 | 0.716 | $0.65^{+0.01}_{-0.01}$ |
| $r_{\rm eff}$ (pc) | $102.1^{+0.2}_{-0.2}$ | $106.2^{+0.5}_{-0.33}$ | $100.3^{+0.1}_{-0.3}$ | $106.44^{+0.2}_{-0.2}$ | $101.15^{+0.11}_{-0.11}$ | $102.26^{+5.11}_{-5.0}$ |
| Sersić (disc/bulge?) | | | | | | |
| Mag | 15.04 | 13.59 | 13.55 | 13.01 | 11.73 | 11.47 |
| PA[c] | $31.53^{+0.04}_{-0.04}$ | $31.0^{+0.03}_{-0.03}$ | $30.22^{+0.03}_{-0.03}$ | $33.9^{+0.03}_{-0.03}$ | $36.46^{+0.02}_{-0.02}$ | $32.59^{+0.11}_{-0.11}$ |
| ell | 0.42 | 0.51 | $0.45^{+0.01}_{-0.02}$ | 0.48 | 0.46 | 0.45 |
| $n$ | 0.97 | 1.13 | 0.99 | 1.044 | 1.214 | 1.102 |
| $r_{\rm eff}$ (pc) | $410.4^{+0.5}_{-1.3}$ | $669.2^{+2.5}_{-1.1}$ | $490.9^{+0.5}_{-0.6}$ | $465.4^{+1.0}_{-1.0}$ | $421.5^{+0.3}_{-0.3}$ | $396.2^{+3.6}_{-5.6}$ |
| Sersić GenEllipse (boxy bulge) | | | | | | |
| Mag | 14.85 | 13.06 | 11.39 | 10.32 | 9.84 | 9.35 |
| PA | $37.47^{+0.02}_{-0.02}$ | $37.05^{+0.02}_{-0.02}$ | $37.18^{+0.07}_{-0.03}$ | $37.79^{+0.17}_{-0.3}$ | $38.40^{+0.3}_{-0.8}$ | $38.98^{+0.05}_{-0.05}$ |
| ell | 0.35 | 0.351 | $0.39^{+0.09}_{-0.09}$ | 0.40 | $0.39^{+0.11}_{-0.04}$ | 0.40 |
| c0 | $1.90^{+0.01}_{-0.01}$ | $1.217^{+0.01}_{-0.01}$ | $0.68^{+0.01}_{-0.0}$ | $0.784^{+0.38}_{-0.29}$ | $1.40^{+0.56}_{-0.57}$ | $1.117^{+0.02}_{-0.02}$ |
| $n$ | 0.52 | $1.35^{+0.01}_{-0.01}$ | $1.83^{+0.01}_{-0.0}$ | $1.613^{+0.36}_{-0.3}$ | $1.36^{+0.23}_{-0.14}$ | $1.49^{+0.01}_{-0.01}$ |
| $r_{\rm eff}$ (pc) | $788.6^{+0.5}_{-0.5}$ | $776.8^{+2.66}_{-2.38}$ | $1182.4^{+0.6}_{-0.5}$ | $925.99^{+10.7}_{-4.5}$ | $937.3^{+0.1}_{-0.1}$ | $1021^{+4.1}_{-3.9}$ |
| Exponential GenEllipse (disc) | | | | | | |
| Mag | 13.66 | 11.84 | 11.71 | 10.17 | 9.62 | 10.35 |
| PA | 35.2 | 38.464 | 36.39 | $37.95^{+0.1}_{-0.1}$ | $38.4^{+0.06}_{-0.04}$ | $38.65^{+0.04}_{-0.04}$ |
| ell | 0.75 | 0.813 | 0.96 | $0.94^{+0.08}_{-0.36}$ | $0.94^{+0.10}_{-0.17}$ | 0.902 |
| c0 | $-1.05^{+0.01}_{-0.01}$ | −1.028 | $2.07^{+0.04}_{-0.03}$ | $1.27^{+0.02}_{-0.08}$ | $1.07^{+0.62}_{-0.08}$ | $1.278^{+0.161}_{-0.139}$ |
| $h$ (kpc)[d] | $2.86^{+0.01}_{-0.01}$ | $4.68^{+0.01}_{-0.01}$ | $5.92^{+0.01}_{-0.01}$ | $6.58^{+0.05}_{-0.15}$ | 6.38 | $2.65^{+0.73}_{-0.70}$ |

*Notes*. [a]Magnitudes are corrected for Galactic reddening only. Intrinsic self-absorption values are obtained via SED fitting in Section 3.3.
[b]Size given in pc or kpc is for an assumed distance of 20.7 Mpc. We calculate $r_{\rm eff}$, from $r_c$, $c$, $\alpha$ of the modified King model as given in Section D.
[c]If PA or ellipticity is not given, their values are 0. If a parameter has no uncertainty, its value is below 1%.
[d]We caution that due to fitting only the inner 1 kpc, the exponential disc scale height might not be truly representative for the actual extent of the disc.

required two Sérsic components for the fit around the NSC (cf. Fig. 4), while the large-scale boxy bulge and disc were fitted with generalized elliptical Sérsic and exponential profiles (see Erwin 2015, and IMFIT manual). We experimented with other functions, including nuclear ring and disc, pure Gaussian, and Core-Sérsic models; however, we achieved worse fits. It was clear from this exploration that the aforementioned components gave the smallest residuals and best-fitting values compared to choosing others or using less or more fitting functions. To illustrate the need for using more components, in Fig. 7 we show the $K_S$-band residual image fitted either without the inner Sérsic ($r_{\rm eff} \sim 100$ pc $\simeq 1$ arcsec) or the outer Sérsic ($r_{\rm eff} \sim 400$ pc $\simeq 5$ arcsec). It is evident that strong residuals arise due to averaged profile resulting from the fit, which highlights the need for having both. Finally, we used the IMFIT–MCMC module to explore a wider region for the range of the fitted parameters via MCMC. From the posterior distributions we obtained their best values and uncertainties. An example is shown in Appendix C, Fig. C1 for the $K_S$ filter. The results from fitting NGC 6384 inner 3.6 kpc in the $JHK_S$ filters are illustrated in Fig. 8 and the best-fitting parameter values for all, including ACS and WFPC 2 filters, are given in Table 1. The different blocks in the table indicate the different components. The left column of Fig. 8 shows the image in each band (from top to bottom), in the middle is the best-fitting model and in the right is the residual image (model minus data). The dust lane is completely transparent in the $K_S$ image (Fig. 8 bottom right), becomes more opaque with decreasing wavelength towards $H$ and $J$ bands and is well visible in the optical ACS filters (cf. Fig. 5, left). This dusty, disc-like structure is not drastically obscuring the NSC, as it can be seen in Fig. 6 (top), to require severe pixel masking that can hamper the fit of the optical profile (cf Fig. 6 middle). This is further supported by the lack of strong colour gradient (cf Fig. 6 bottom). The colour and its gradient as well as the

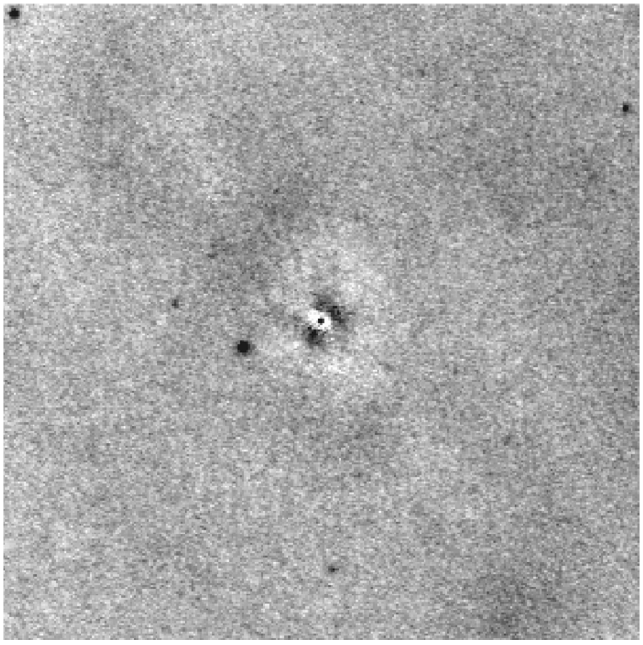

**Figure 7.** $K_S$-band residual image from a model fit either without the inner Sérsic ($r_{\rm eff} \sim 100$ pc $\simeq 1$ arcsec) or the outer Sérsic ($r_{\rm eff} \sim 400$ pc $\simeq 5$ arcsec) components. The result is identical for the other filters and the *HST* images as well.

structure of the various components given in Table 1 is discussed in Section 4.

### 3.3 SED analysis of the central kiloparsec

Here we analyse the SED of NGC 6384 of the overlapping region between our NIR images and the archival *HST* optical data. To closely account for the extended nature and evidently varying structure of the NSC as a function of wavelength, we use its six filter model magnitudes, which unlike fixed aperture magnitudes, should not only account for the varying PSF with wavelength, the varying structure of the cluster, but also minimize contamination from flux coming from the other underlying galactic components. We also model the SED of the SB profile of the inner kiloparsec of NGC 6384 in the six filters, which should well represent its stellar population properties on scales $r \gtrsim 0.12$ arcsec as PSF effects are not taken into account by the Ellipse extraction (see Section 3.2).

Our SED fitting uses a mixture of old and young stellar populations, including nebular emission, fitting for dust extinction, and testing for a weak AGN component. The latter is motivated by the fact that NGC 6384 is similar by mass to the MW and M 31 and its NSC could similarly harbour an MBH of 1–10 million solar mass, which might be more active. Thus, a certain fraction of the flux in the core might be coming from a weak AGN component. NGC 6384 is also classified as a transitional type (T2) LINER (Ho et al. 1997), which further support the need to probe for an AGN. To test for all these components contributing to the SED, we use the CIGALE[10] code (Burgarella, Buat & Iglesias-Páramo 2005; Noll et al. 2009; Roehlly et al. 2014; Boquien et al. 2018). It has been developed to fit the SED of galaxies using various models of the SFH (double exponential, delayed, periodic, and user specified), a choice of SSP model (Bruzual & Charlot 2003; Maraston 2005) with a given IMF, adding dust attenuation (Calzetti, Kinney & Storchi-Bergmann 1994; Calzetti et al. 2000, single or double power law) and possible nebular, AGN (Fritz, Franceschini & Hatziminaoglou 2006; Dale et al. 2014) and dust emission (Draine & Li 2007; Casey 2012; Dale et al. 2014; Draine et al. 2014). We first fitted with CIGALE the SED of the NSC using the six band model magnitudes given in Table 1. We assumed a double exponential SFH to test for the presence of more than one stellar population. Although NSC may experience a prolonged SFH with many episodic bursts of star formation, typically, they host two main stellar populations which contribute, if not to all, to the majority of their current mass and light, i.e. an old (metal-poorer) and a younger and more metal-rich (Rossa et al. 2006; Seth et al. 2006; Walcher et al. 2006; Kacharov et al. 2018). Under this assumption of two main bursts of star formation, we modified the BC03 module of CIGALE to allow for the old and young population to be constructed from SSPs with different metallicity.

Allowing for a wide range of possible parameter values for all aforementioned SED components, resulted in the synthesis of 403200 SEDs. CIGALE analyses all these models compared to the observed SED in a Bayesian framework, i.e. calculating the probability of each model given the data, and constructing posterior distributions for each model parameter from which their best value and uncertainties are obtained (details in Burgarella et al. 2005; Boquien et al. 2018). We show the best fit SED of the NSC in Fig. 9, where all fitted components are given in the figure legend. The main properties from the six band optical-NIR SED fitting are summarized in Table 2. We did not include the AGN fraction of the fit into the table, as its contribution (if any) is very small, $< 1$ per cent (0.46 per cent $\pm$ 0.36 per cent), and a geometry of a minimum to maximum radii of the dusty torus of $r = 60 \pm 3$ with an opening angle $\Theta = 100^\circ \pm 40^\circ$ and an angle between the AGN and the line of sight of $\psi = 70.1^\circ \pm 3.5^\circ$. We further comment on this in Section 4.

As a consistency check, instead of using the NSC model magnitudes, we used a fixed aperture NSC magnitudes with a diameter of 0.35 arcsec. This is large enough to avoid PSF effects, contain light mostly from the NSC whose diameter is smaller than that, as well as it is small enough to minimize contaminating flux from the underlying structures. The result from fitting the NSC SED using the aperture magnitudes is that the NSC age of both populations remained unchanged (1 per cent lower); the NSC total mass decreased by ∼47 per cent, largely driven by the lower mass of the old population (by 52 per cent) due to the inclusion of contaminating flux from the likely younger underlying disc stellar population that lower the *M*/*L*. Respectively, the metallicity and attenuation values also lowered by up to ∼45 per cent. To conclude, the stellar population values for both populations obtained from fixed aperture are within the measurement uncertainties given in Table 2; however, as expected, there is a systematic bias due to the contaminating flux from the underlying disc/bulge components in direction of their respective stellar population properties. This result will hold true only for aperture magnitudes obtained from high spatial resolution observations allowing the extraction of NSC photometry from an aperture big enough to avoid PSF affects across different filters, but small enough to minimize contamination. Obviously, the latter will also strongly depend on the structure and profile of the underlying components.

To obtain a radial map of the stellar population properties, we also fit the SED at each radial location along the SB profile of all filters extracted with ELLIPSE. A summary from this fitting we show

[10]We used version 0.12.1 cigale.lam.fr

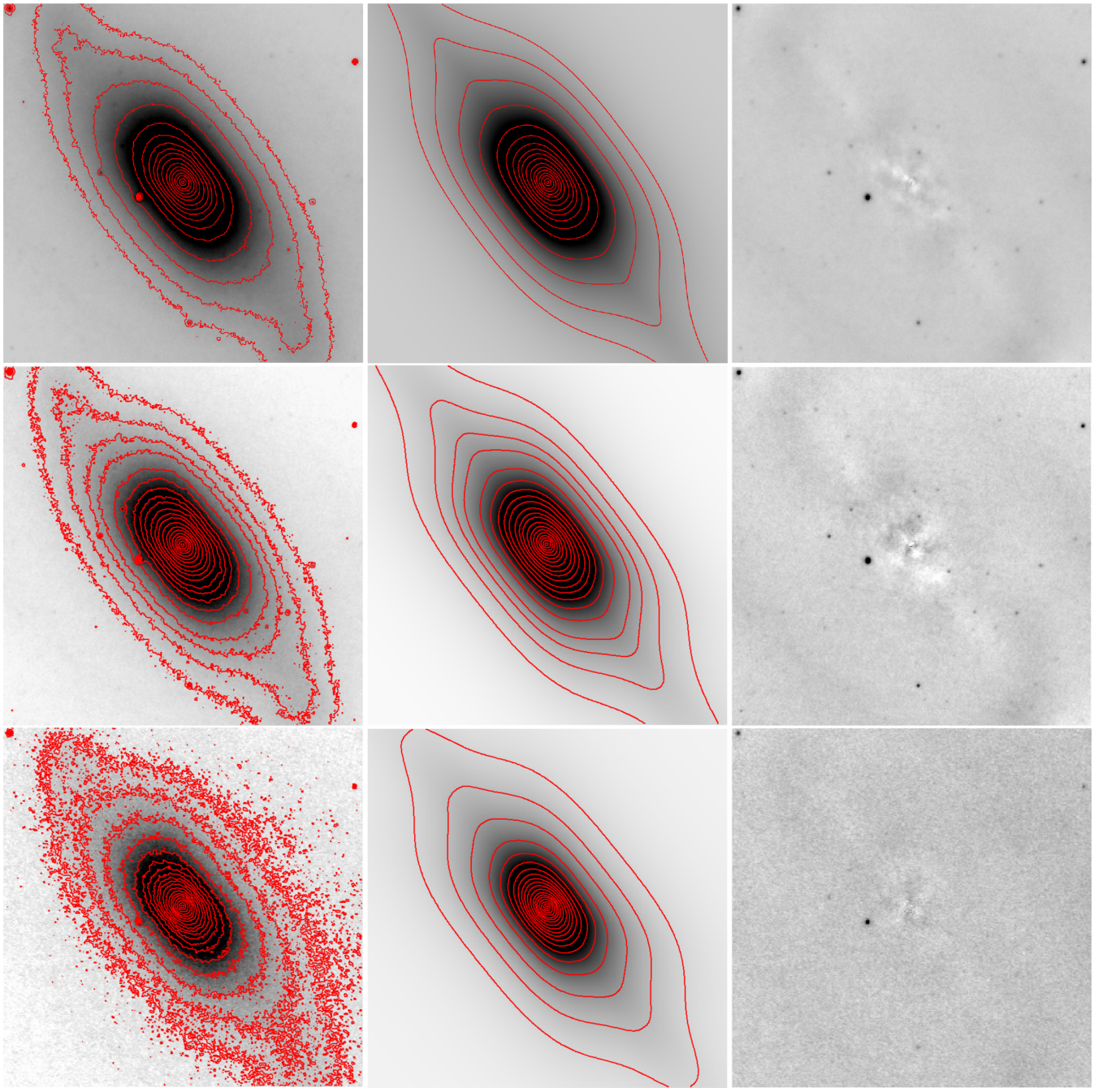

**Figure 8. Top to bottom:** $J, H, K_S$ NGC 6384 images (**left column**) of the central 3.6 × 3.6 kpc (∼36 × 36 arcsec). **Middle:** Best-fitting model and **right column** is the residual image (model minus the data). For reference and to guide the eye, we show them with red contours the data and model images at same isophotal levels.

in Fig. 10 of the one-dimensional projection along the semimajor axis of the main properties of the two stellar populations: stellar surface mass density, metallicity, and fraction of the young stellar population, from top to bottom, respectively. For comparison, with an asterisk in Fig. 10 we also show the integrated values of the NSC from Table 2, at the mean radial location of its effective radius from all filters of 10 pc. All other relevant parameters [$E(B-V)$, age, e-folding time of the two stellar population] from the SED fitting did not show significant (or interesting) radial gradients. We note that although we extracted the radial SB beyond the 10 per cent of the $\mathrm{PSF_{FWHM}}$, the very central 2–3 radial points ($\lesssim$0.07 arcsec) in Fig. 10 might not be fully representative and still suffer from differential PSF effects between the *HST* and the LUCI + ARGOS images.

## 4 DISCUSSION

Here we discuss our main findings on the properties of the NSC of NGC 6384, an MW like galaxy. Enabled by the sharp (0.25 arcsec) and stable PSF provided by ARGOS across the 4 × 4 arcmin LUCI 2 field of view (Section B) we analyse the central 3.6 × 3.6 kpc (∼36 × 36 arcsec) overlap region between our NIR LBT and archival

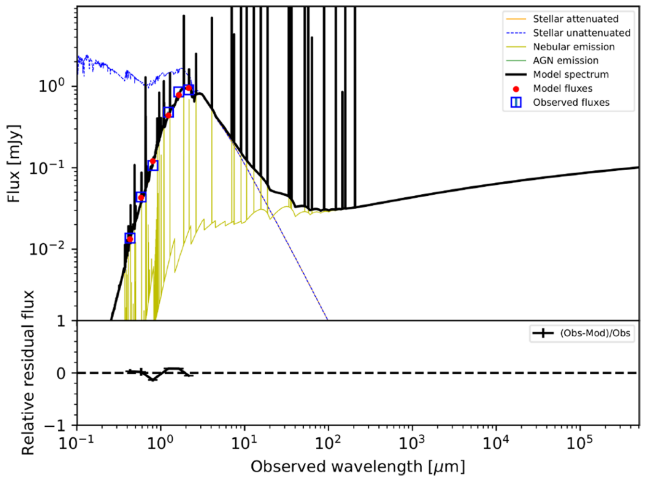


**Figure 9.** The best SED fit to the NGC 6384 NSC using six-band optical-NIR photometry (*HST*: *F*450*W*, *F*606*W*, *F*814*W*, and LBT/LUCI: *J*, *H*, $K_S$). The fluxes are from the model magnitudes in Table 1 obtained via 2D image modelling (in Section 3.2). SED fitting details in Section 3.3.

**Table 2.** Properties of the NSC from SED fitting (in Section 3.3) to the six filter optical-NIR model magnitudes in Table 1.

| Population | Age (Gyr) | Metallicity, [M/H] (dex) | $E(B-V)$ (mag) | Mass ($10^6$ $M_\odot$) |
|---|---|---|---|---|
| Old | $10.85 \pm 1.33$ | $-0.11 \pm 0.16$ | $0.63 \pm 0.15$ | $35.3 \pm 21.6$ |
| Young | $0.23 \pm 0.14$ | $0.33 \pm 0.13$ | $1.44 \pm 0.33$ | $2.86 \pm 1.9$ |

optical *HST* data. The high spatial resolution in the NIR is crucial for breaking age–metallicity–reddening degeneracies when combined with the optical *HST* data.

### 4.1 The NSC embedded in nuclear (disc) components

The 2D image fitting of the high spatial resolution NIR LUCI 2 and optical *HST* images allowed us to uncover the presence of two inner Sersić components (Section 3.2, Fig. 4) with effective radii of ∼100 and 400 pc in which the NSC with $r_{\rm eff} \simeq 10$ pc is embedded. We also successfully fitted for the large-scale boxy bulge ($r_{\rm eff} \sim 1$ kpc) and disc (∼6 kpc). The properties of these multiple components are given in Table 1. The two inner Sersić profiles have low Sersic indices ($n \simeq 0.75$ and $\simeq 1$), which suggests that these might be nuclear discs. Similar central discs are observed in the MW as well as in other galaxies. For example, stellar line-of-sight velocity distributions of stars in the MW reveals a nuclear disc of a truncation radius of ∼150 pc (e.g. Schönrich, Aumer & Sale 2015). In other galaxies, observations with sufficiently high spatial resolution shows that their central zones also contain nuclear discs (e.g. Balcells et al. 2003; Seth et al. 2006; Balcells, Graham & Peletier 2007; Ganda et al. 2009; Méndez-Abreu et al. 2017). Their formation, in the case of the MW, is reproduced by *N*-body + smooth particle hydrodynamics simulations (Debattista et al. 2015, 2018), which form a nuclear disc (or ring) during bar-induced gas inflows (Cole et al. 2014). In other galaxies, similar process of star formation in nuclear rings is suggested to form nuclear discs (e.g. Kormendy & Kennicutt 2004). This implies that the (few) hundred parsecs components around the NSC of NGC 6384 are common in galaxies. However, the fact that we observe two in NGC 6384 might

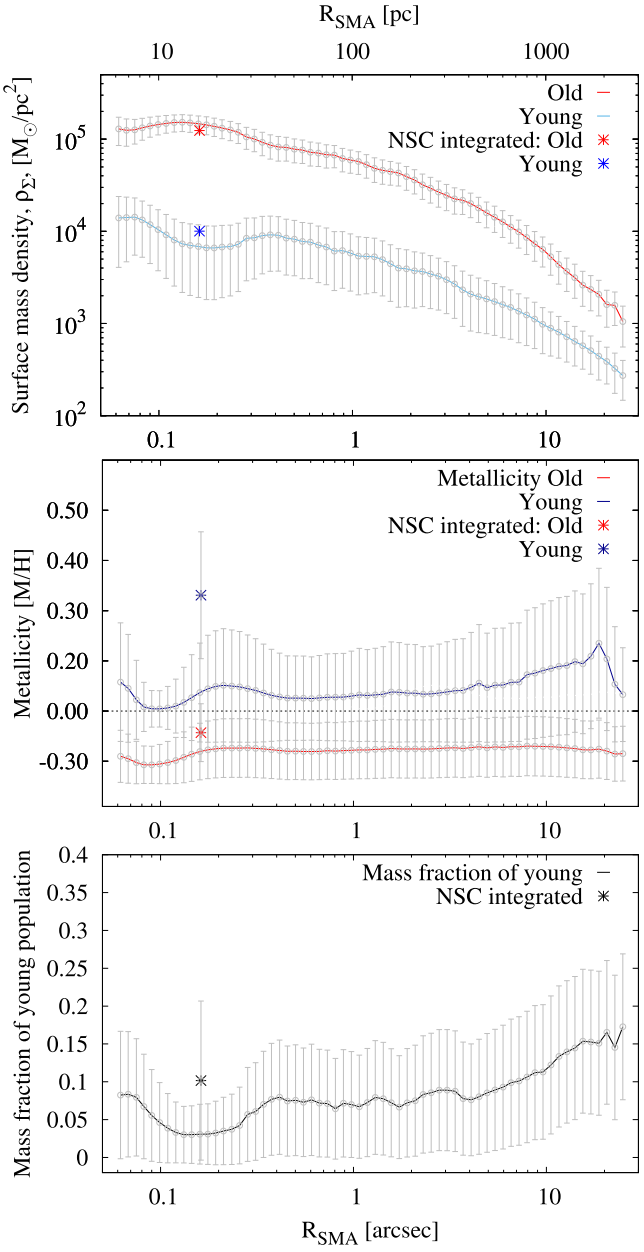


**Figure 10.** Radial map of the SED modelled composite stellar population. From top to bottom are shown the stellar mass, metallicity, and mass fraction of the young stellar population.

hint at specific events in the formation past of its central regions and their eventual timing. For example, star cluster merger simulations do form nuclear discs of similar scales, which are also suggested to be useful for timing past merger events (e.g. Portaluri et al. 2013; Sarzi et al. 2016; Arca-Sedda & Capuzzo-Dolcetta 2016, 2017).

### 4.2 NSC effective radius varying with wavelength

We observe that the effective radius of NGC 6384 NSC is larger at longer wavelengths. This is illustrated in Fig. 11, alongside with the other fitted components, except for the large-scale exponential disc, which extent is well beyond our fitting area and thus might not be fully representative. Fig. 11 shows the ratio between the effective radius in the $K_S$ band, as a base, and that in the other filters. Especially

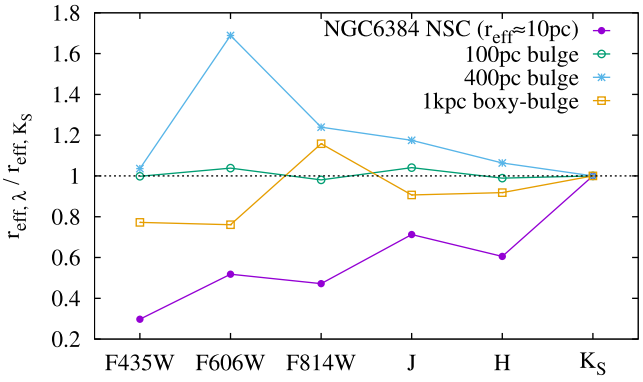


**Figure 11.** Ratio between the effective radius in $K_S$ band to that in the other filters for each structural component.

for the NSC, we see that it becomes significantly more compact in *F435W* (*B* band) which suggests for a more centrally concentrated younger stellar population, as observed also in other studies (Seth et al. 2008; Georgiev & Böker 2014; Carson et al. 2015). On average, the $r_{\rm eff}$ 100 pc bulge size is fairly invariant, while the 400 pc bulge size is increasing with decreasing wavelength peaking in *F606W*. This filter also contains the *H* $\alpha$ line, which could be driving its very large size. Its very compact size in *F435W* supports the presence of more centrally concentrated young population. The NGC 6384 boxy bulge also shows steadily decreasing effective radius with decreasing wavelength. This implies that it is mainly composed of old stellar population. As the main focus of this paper is on the NSC of NGC 6384 would not like to extend our discussion to the bulge/pseudo-bulge topic.

The structural reanalysis of the *HST* WFPC 2 *F606W* image, which we presented in Georgiev & Böker (2014), showed that not accounting for the inner components led to an overestimate of the NSC effective radius by ∼30 per cent and its magnitude by ∼0.4 mag. Overall, this might not represent a drastic bias (roughly 0.4 dex biased mass estimate); however, the ability to resolve and model all components in the central regions is essential for the correct mass and dynamical modelling of the NSC and its surroundings when future spectroscopy is included.

### 4.3 NSC stellar population from the SED analysis

Using the six band photometry, we perform in Section 3.3 an SED fitting to the model magnitudes of the NSC (Fig. 9) as well as the to the SB-profile of NGC 6384 (Section 10). We find that the NIR and optical data helped to leverage the age–metallicity–extinction degeneracies and derive the effective NSC stellar population properties (cf. Table 2). As typically observed in NSCs most of the mass/light is contained in two populations of young and old age, the latter ≃90 per cent by mass (e.g. Seth et al. 2006), we find for the NGC 6384 NSC an old component with an age of 10.8 ± 1.3 Gyr and a stellar mass of $\mathcal{M}_{\star,\rm NSC,old} = 3.5 \times 10^7\,{\rm M}_\odot$. A young component has an age of 230 ± 140 Myr, which is ∼8 per cent of the mass of the old population. The e-folding time for the old and young population is 2.3 and 0.14 Gyr, respectively. The old and young stellar populations have slightly sub- and supersolar metallicity, which is in line with spectroscopic metallicity measurements of other extragalactic NSCs. However, because our SED fitting can report only for the total metal content (*Z*/*H*), therefore the metallicity values in Table 1 are strong upper limits to the Fe abundance.

The radial map of the NSC surface mass density, age, metallicity, and reddening (cf. Fig 10) follow trends consistent with the aforementioned breakdown of the stellar population of the NSC. The extinction value of $E(B-V) \simeq 1$ mag, i.e. $A_V \simeq 4$ mag is expectedly, much lower than that towards the Galactic centre, due to the lower inclination of NGC 6384 nucleus, compared to the line of sight towards the MW NSC. The reddening values found here are in agreement with the range found for the nuclear regions of other galaxies from optical-NIR photometric analysis (e.g. Ganda et al. 2009; Carson et al. 2015).

### 4.4 Insufficient evidence for AGN activity

The SED fitting resulted in negligible, <1 per cent fraction of the light ($\lesssim 10^4$ erg s$^{-1}$), to be coming from a weak AGN activity. This would be the upper limit on the possible AGN contribution to the NSC SED. We have only six SED points, which still leaves the possibility of a weak AGN component, however, its geometry has to have a more extreme configuration than the one found here (cf Section 3.3). Any present degeneracies should be reflected in the uncertainty ranges obtained from the posteriors by CIGALE. Also, if the AGN fraction is higher, instead of a contribution from younger stellar population, this would lead to a steeper SED continuum shape in the NIR (redder colour), and will require lower reddening. However, this will be inconsistent with the overall optical-NIR SED shape, as investigated observationally by SED studies at pc scales to identify AGN contributions (e.g. Prieto et al. 2010). This highlights the power of combining optical and NIR that covers one of the most important wavelength ranges for minimizing various of the aforementioned degeneracies. Therefore, this data cannot support an active MBH in the NSC of NGC 6384. This, however, does not exclude the presence of a MBH, because it might not be in an active state, just like the one in the MW and M 31. A follow up high spatial and spectral resolution NIR spectroscopy is needed to measure the NSC and its central velocity dispersion to assess the presence of a MBH. The lack of clear AGN component in our SED fitting and the indications for very centrally concentrated young stellar population as discussed earlier (cf. Fig. 11) suggests that the LINER emission of the nucleus of NGC 6384 measured in low-spatial resolution (2.5 arcsec spectra) is likely due to the young star formation activity in its central regions rather than an AGN activity.

### 4.5 Implications for the formation of NGC 6384 NSC

Finally, the evidences from our measurements of the NGC 6384 NSC having an effective radius as extended as $r_{\rm eff} \simeq 10$ pc and varying with wavelength, two circum nuclear Sersić components of 100 and 400 pc scales and low $n$ − indices consistent with being nuclear discs, the non-negligible by mass young stellar component and the clear detection of disc-like dust lane spiralling into the cluster shares features of the two main scenarios of NSC formation: (*i*) cluster merging, which leads to larger effective radii and possible formation of nuclear discs (see Section 4.1) (*ii*) repetitive gas accretion which leads to the presence of young stellar population (see Section 4.3). This finding for NGC 6384 NSC adds to the growing body of evidence in the literature that supports not a single formation channel during the build-up of galactic nuclei, but a complex and individual mixture of both. A larger, representative sample of galactic nuclei analysed in such manner can allow for a more systematic and statistically meaningful conclusions about the build-up of galactic nuclei depending on galaxy mass, type, environment, and whether the nucleus is co-inhabited by an MBH.

## 5 SUMMARY

Here we presented the analysis of the first science data taken during the commissioning of the ARGOS system in 2015-05-01 and 02. It provides adaptive optics correction of the ground atmospheric layer at the LBT. The target for this commissioning run, NGC 6384 was mainly selected because it has a suitable on-axis AO reference star and a large number of MW stars to measure system performance. The fact that this galaxy was at a large distance of 20.7 Mpc allowed us to also demonstrate that star cluster science can be conducted successfully, where ground based seeing limited observations lack the needed spatial resolution to study such compact stellar systems.

For the proper analysis of the NIR images with the LUCI 2 camera, which suffers from persistence and non-linearity effects, we created pixel-to-pixel maps that we used to pre-process and correct the raw images (details in Section A). Following standard data reduction steps (Section 2.1) and calibration, we were able to achieve excellent image registration resulting in a sharp and stable PSF of 0.25 arcsec over the entire 4 × 4 arcmin LUCI 2 field of view. The PSF size only increases by $\lesssim$25 per cent out to the detector edges (Section B). This superb spatial resolution enables to resolve the star cluster candidates and bring down contamination from background galaxies to a minimum. In a forthcoming paper we will present the detailed analysis of the star cluster system of NGC 6384 (cf Section 3.1), while in this paper we mainly focus our analysis to the central 3.6 × 3.6 kpc (∼36 × 36 arcsec) overlap region between our NIR LBT and archival optical *HST* data. The high spatial NIR imaging is crucial for breaking age–metallicity–reddening degeneracies when combined with the optical *HST* data. We reprocessed the *HST*/ACS and WFPC 2 data to the same plate scale resolution of 0.05 arcsec pixel$^{-1}$ (cf. Section 2.2).

We performed a 2D MCMC image fitting with IMFIT (Erwin 2015) by using a PSF model built from stars in the image for both the LUCI 2 and *HST* images, as well as a TINYTIM (Krist et al. 2011) PSF model drizzled in identical manner as the science images. We also used a pixel mask of the central obscuring disc-like dust lane (Section 3.2, Fig. 5).

Our main findings can be summarizes as follows:

(i) We uncover the presence of two inner Sersić (low $n$ − index, disc?) components (Section 3.2, Fig. 4 and Section 4.1) with effective radii of ∼100 and 400 pc in which the NSC with $r_{\rm eff} \simeq 10$ pc is embedded. NGC 6384 has a large-scale boxy bulge (∼1 kpc) and disc (∼6 kpc).

(ii) The effective radius of NGC 6384 NSC increases with wavelength (cf. Fig. 11, which suggests for a more centrally concentrated younger stellar population (see Section 4.2).

(iii) The NSC effective radius is smaller in size by ∼30 per cent and magnitude/mass by ∼0.4 mag/dex compared to Georgiev & Böker (2014) due to the unaccounted inner Sersić components. This highlights the need to resolve and model well the central regions for the correct mass and dynamical modelling of the NSC when follow-up spectroscopy is included.

(iv) The NSC SED is described by an old population (10.8 ± 1.3 Gyr) with a stellar mass of $\mathcal{M}_{\star,\rm NSC,old} = 3.5 \times 10^7\,{\rm M}_\odot$, and a young population of 230 ± 140 Myr, which is ∼8 per cent of its mass. Both populations have slightly sub- and supersolar metallicity, respectively (cf. Table 2, Sections 3.3 and 4.3).

(v) We obtained the SED radial surface mass density, age, metalicity, and reddening (cf. Fig 10, Sections 3.3 and 4.3)

(vi) We find negligible, <1 per cent fraction of the light, to be coming from a weak AGN (Section 4.4). If an MBH in the NSC of NGC 6384 is present, then it might not be accreting, similarly to those in the MW and M 31.

(vii) All structural and stellar population evidences suggest that the NGC 6384 NSC for a formation contributed from the two-main scenarios of NSC formation: cluster merging and repetitive gas accretion.

## ACKNOWLEDGEMENTS

We thank the anonymous referee for their constructive and useful comments that helped to improve parts of the discussion in the paper. Based on observations collected at the Large Binocular Telescope (LBT). The LBT is an international collaboration among institutions in the United States, Italy and Germany. LBT Corporation partners are: The University of Arizona on be- half of the Arizona Board of Regents; Istituto Nazionale di Astrofisica, Italy; LBT Beteiligungsgesellschaft, Germany, representing the Max-Planck Society, The Leibniz Institute for Astrophysics Potsdam, and Heidelberg University; The Ohio State University, and The Research Corporation, on behalf of The University of Notre Dame, University of Minnesota and University of Virginia. This research has made use of the NASA/IPAC Extragalactic Data Base (NED), which is operated by the by the Jet Propulsion Laboratory, California Institute of Technology, under contract with the National Aeronautics and Space Administration (NASA). We also acknowledge the use of HyperLEDA database (http://leda.univ-lion1.fr, the VizieR catalogue access and the 'Aladin sky atlas' tools developed at CDS, Strasbourg, France.

## REFERENCES

Abbott C. G., Valluri M., Shen J., Debattista V. P., 2017, MNRAS, 470, 1526
Antonini F., Barausse E., Silk J., 2015, ApJ, 806, L8
Antonini F., Capuzzo-Dolcetta R., Mastrobuono-Battisti A., Merritt D., 2012, ApJ, 750, 111
Arca-Sedda M., Capuzzo-Dolcetta R., 2016, preprint (arXiv:1601.04861)
Arca-Sedda M., Capuzzo-Dolcetta R., 2017, MNRAS, 471, 478
Astropy Collaboration, 2013, A&A, 558, A33
Astropy Collaboration, 2018, AJ, 156, 123
Athanassoula E., Beaton R. L., 2006, MNRAS, 370, 1499
Balcells M., Graham A. W., Domínguez-Palmero L., Peletier R. F., 2003, ApJ, 582, L79
Balcells M., Graham A. W., Peletier R. F., 2007, ApJ, 665, 1084
Beaton R. L. et al., 2007, ApJ, 658, L91
Bekki K., 2007, PASA, 24, 77
Bekki K., Couch W. J., Drinkwater M. J., Shioya Y., 2004, ApJ, 610, L13
Boquien M., Burgarella D., Roehlly Y., Buat V., Ciesla L., Corre D., Inoue A. K., Salas H., 2018, preprint (arXiv:1811.03094)
Bruzual G., Charlot S., 2003, MNRAS, 344, 1000
Burgarella D., Buat V., Iglesias-Páramo J., 2005, MNRAS, 360, 1413
Böker T., Laine S., van der Marel R. P., Sarzi M., Rix H.-W., Ho L. C., Shields J. C., 2002, AJ, 123, 1389
Böker T., Lisenfeld U., Schinnerer E., 2003, A&A, 406, 87
Böker T., Sarzi M., McLaughlin D. E., van der Marel R. P., Rix H.-W., Ho L. C., Shields J. C., 2004, AJ, 127, 105
Calzetti D., Armus L., Bohlin R. C., Kinney A. L., Koornneef J., Storchi-Bergmann T., 2000, ApJ, 533, 682
Calzetti D., Kinney A. L., Storchi-Bergmann T., 1994, ApJ, 429, 582
Capuzzo-Dolcetta R., 1993, ApJ, 415, 616
Carson D. J., Barth A. J., Seth A. C., den Brok M., Cappellari M., Greene J. E., Ho L. C., Neumayer N., 2015, AJ, 149, 170
Casey C. M., 2012, MNRAS, 425, 3094

Cole D. R., Debattista V. P., Erwin P., Earp S. W. F., Roškar R., 2014, MNRAS, 445, 3352
Cole D. R., Debattista V. P., Varri A.-L., Adam M., Seth A. C., 2017, MNRAS, 466, 2895
Dale D. A., Helou G., Magdis G. E., Armus L., Díaz-Santos T., Shi Y., 2014, ApJ, 784, 83
Dale D. A. et al., 2016, AJ, 151, 4
Debattista V. P., Earp S. W. F., Ness M., Gonzalez O. A., 2018, MNRAS, 473, 5275
Debattista V. P., Ness M., Earp S. W. F., Cole D. R., 2015, ApJ, 812, L16
de Meulenaer P., Narbutis D., Mineikis T., Vansevičius V., 2014, A&A, 569, A4
Draine B. T., Li A., 2007, ApJ, 657, 810
Draine B. T. et al., 2014, ApJ, 780, 172
Drouart G., Rocca-Volmerange B., De Breuck C., Fioc M., Lehnert M., Seymour N., Stern D., Vernet J., 2016, A&A, 593, A109
Dwek E. et al., 1995, ApJ, 445, 716
Elson R. A. W., 1999, in Martínez Roger C., Perez Fournón I., Sánchez F., eds, Globular Clusters, Cambridge University Press, Cambridge, UK, p. 209
Erwin P., 2015, ApJ, 799, 226
Erwin P., Debattista V. P., 2013, MNRAS, 431, 3060
Erwin P., Debattista V. P., 2017, MNRAS, 468, 2058
Feldmeier-Krause A., Zhu L., Neumayer N., van de Ven G., de Zeeuw P. T., Schödel R., 2017, MNRAS, 466, 4040
Feldmeier A. et al., 2014, A&A, 570, A2
Fellhauer M., Kroupa P., 2002, MNRAS, 330, 642
Fitzpatrick E. L., 1999, PASP, 111, 63
Foreman-Mackey D., 2016, J. Open Source Softw., 24
Fritz J., Franceschini A., Hatziminaoglou E., 2006, MNRAS, 366, 767
Ganda K., Peletier R. F., Balcells M., Falcón-Barroso J., 2009, MNRAS, 395, 1669
Georgiev I. Y., Böker T., 2014, MNRAS, 441, 3570
Georgiev I. Y., Böker T., Leigh N., Lützgendorf N., Neumayer N., 2016, MNRAS, 457, 2122
Georgiev I. Y., Goudfrooij P., Puzia T. H., 2012, MNRAS, 420, 1317
Georgiev I. Y., Goudfrooij P., Puzia T. H., Hilker M., 2008, AJ, 135, 1858
Gravity Collaboration, 2018, A&A, 615, L15
Hartmann M., Debattista V. P., Seth A., Cappellari M., Quinn T. R., 2011, MNRAS, 418, 2697
Hill J. M., 1994, American Astronomical Society Meeting Abstracts, p. 1322
Hill J. M., Green R. F., Ashby D. S., Brynnel J. G., Cushing N. J., Little J. K., Slagle J. H., Wagner R. M., 2012, in Stepp L. M., Gilmozzi R., Hal H. J., eds, Proc. SPIE Conf. Ser., Vol. 8444. Ground-based and Airborne Telescopes IV. SPIE, Bellingham, p. 84441A
Ho L. C., Filippenko A. V., Sargent W. L. W., 1997, ApJS, 112, 315
Häring-Neumayer N., Cappellari M., Rix H. W., Hartung M., Prieto M. A., Meisenheimer K., Lenzen R., 2006, ApJ, 643, 226
Kacharov N., Neumayer N., Seth A. C., Cappellari M., McDermid R., Walcher C. J., Böker T., 2018, MNRAS, 480, 1973
King I., 1962, AJ, 67, 471
Kormendy J., Kennicutt Robert C. J., 2004, ARA&A, 42, 603
Krist J. E., Hook R. N., Stoehr F., 2011, in Kahan M. A., ed., SPIE Conf. Ser., Vol. 8127. Optical Modeling and Performance Predictions V. SPIE, Bellingham
Larsen S. S., 1999, A&AS, 139, 393
Laurikainen E., Salo H., Buta R., Knapen J. H., 2011, MNRAS, 418, 1452
Makarov D., Prugniel P., Terekhova N., Courtois H., Vauglin I., 2014, A&A, 570, A13
Maraston C., 2005, MNRAS, 362, 799
McWilliam A., Zoccali M., 2010, ApJ, 724, 1491
Milosavljević M., 2004, ApJ, 605, L13
Méndez-Abreu J. et al., 2017, A&A, 598, A32
Ness M., Lang D., 2016, AJ, 152, 14
Neumayer N., Walcher C. J., 2012, Adv. Astron., 2012, 709038
Neumayer N., Walcher C. J., Andersen D., Sánchez S. F., Böker T., Rix H.-W., 2011, MNRAS, 413, 1875
Nguyen D. D. et al., 2018, ApJ, 858, 118
Noll S., Burgarella D., Giovannoli E., Buat V., Marcillac D., Muñoz-Mateos J. C., 2009, A&A, 507, 1793
Oh K. S., Lin D. N. C., 2000, ApJ, 543, 620
Ordenes-Briceño Y. et al., 2018, ApJ, 860, 4
Peng C. Y., Ho L. C., Impey C. D., Rix H.-W., 2010, AJ, 139, 2097
Portaluri E., Corsini E. M., Morelli L., Hartmann M., Dalla Bontà E., Debattista V. P., Pizzella A., 2013, MNRAS, 433, 434
Prieto M. A., Reunanen J., Tristram K. R. W., Neumayer N., Fernandez-Ontiveros J. A., Orienti M., Meisenheimer K., 2010, MNRAS, 402, 724
Rabien S. et al., 2018, A&A, 621, A4
Roehlly Y., Burgarella D., Buat V., Boquien M., Ciesla L., Heinis S., 2014, in Manset N., Forshay P., eds, ASP Conf. Ser., Vol. 485, Astronomical Data Analysis Software and Systems XXIII. Astron. Soc. Pac., San Francisco, p. 347
Rossa J., van der Marel R. P., Böker T., Gerssen J., Ho L. C., Rix H.-W., Shields J. C., Walcher C.-J., 2006, AJ, 132, 1074
Sarzi M. et al., 2016, MNRAS, 457, 1804
Schinnerer E., Böker T., Emsellem E., Lisenfeld U., 2006, ApJ, 649, 181
Schinnerer E., Böker T., Meier D. S., 2003, ApJ, 591, L115
Schlafly E. F., Finkbeiner D. P., 2011, ApJ, 737, 103
Schlegel D. J., Finkbeiner D. P., Davis M., 1998, ApJ, 500, 525
Schödel R., Feldmeier A., Kunneriath D., Stolovy S., Neumayer N., Amaro-Seoane P., Nishiyama S., 2014, A&A, 566, A47
Schödel R. et al., 2007, A&A, 469, 125
Schönrich R., Aumer M., Sale S. E., 2015, ApJ, 812, L21
Seifert W. et al., 2003, in Iye M., Moorwood A. F. M., eds, SPIE Conf. Ser., Vol. 4841. Instrument Design and Performance for Optical/Infrared Ground-based Telescopes. SPIE, Belligham, p. 962
Seth A. C., Blum R. D., Bastian N., Caldwell N., Debattista V. P., 2008, ApJ, 687, 997
Seth A. C., Dalcanton J. J., Hodge P. W., Debattista V. P., 2006, AJ, 132, 2539
Seth A. C. et al., 2010, ApJ, 714, 713
Sorce J. G., Tully R. B., Courtois H. M., Jarrett T. H., Neill J. D., Shaya E. J., 2014, MNRAS, 444, 527
Sánchez-Janssen R. et al., 2018, preprint (arXiv:1812.01019)
Tremaine S. D., Ostriker J. P., Spitzer L., Jr., 1975, ApJ, 196, 407
Tsang B. T. H., Milosavljević M., 2018, MNRAS, 478, 4142
Tsatsi A., Mastrobuono-Battisti A., van de Ven G., Perets H. B., Bianchini P., Neumayer N., 2017, MNRAS, 464, 3720
Walcher C. J., Böker T., Charlot S., Ho L. C., Rix H.-W., Rossa J., Shields J. C., van der Marel R. P., 2006, ApJ, 649, 692
Walcher C. J. et al., 2005, ApJ, 618, 237

## APPENDIX A: LUCI 2 LINEARITY AND PERSISTENCE MAPS

The first linearity and persistence analysis of the LUCI 2 N 3.75 detector was performed by David Thompson (at LBTO) that is available at the LUCI 2 webpage.[11] This linearity correction needs to be applied to the counts of all raw data prior any data reduction. The coefficients for this correction are estimated for the detector average pixel values, which can be a good overall correction. However, often (if not exclusively), science measurements are made on a small pixel area of the detector, which could (significantly) deviate from the detector average linearity coefficients and compromise scientific flux and position measurements. Therefore, we performed a new pixel-by-pixel linearity, and not quantified so far, persistence analysis of the LUCI 2 N 3.75 camera. For that we used linearity data taken and kindly provided to us by David Thompson. The data

[11] http://scienceops.lbto.org/sciops_cookbook/luci2-versus-luci1/#L2vL1_Nonlinearity

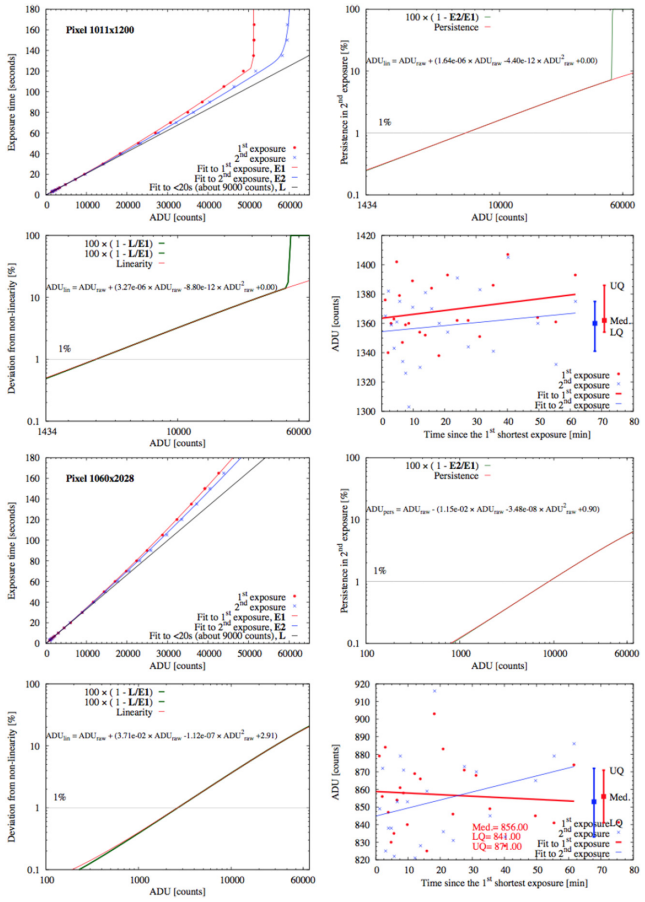


**Figure A1.** An example for the pixel-by-pixel linearity and persistence solutions for the LUCI 2 detector. **Top four** and **bottom four** panels show an example of two pixels at different location on the detector that show different linearity and persistence curves. For each group of four panels, from **top-left** to **bottom-right** clockwise, are shown the exposure time as a function of pixel value (shown this way for fitting purposes), the linearity, the persistence, and the noise statistics of that pixels as a function of the time during which the linearity data were taken. Lines with solid circles and crosses in **top-left** panel show the first and second exposure taken in a sequence until saturation is reached and their fitted functions, as indicated in the panel legend. **Top-right** and **bottom-left** panels show the ratio of the fitted functions and their coefficients are shown with label in the panels. **Bottom-right** panels show the pixel value of the 1st and 2nd exposure in the sequence.

consist of a sequence of images with increasing exposure time until detector saturation is reached. Two consecutive frames are taken at the same exposure time to allow to analyse detector persistence. For the analysis, we extract the count value of every pixel and exposure and fit curves to the 1st and 2nd exposures as a function exposure time.

We confirm results from earlier analysis that departures from linearity $\gtrsim$5 per cent occur at around 9000 counts. Therefore, to set the linearity reference line we perform a least-squares fit of a linear form to the count values of the 1st exposure smaller than 9000 counts. The ratio between the curves of the 1st exposure and that of the linear region provides the linearity correction relation. The ratio between the fitted curves for the 1st and 2nd exposure sets as a function of the count rate provides the relation for the persistence correction. Each of these fits and ratios, for the persistence and linearity, are shown in Fig. A1. To demonstrate

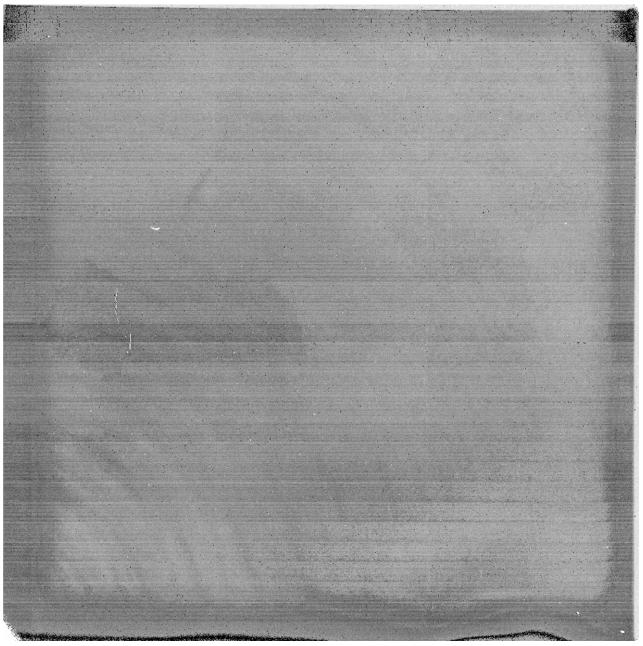

**Figure A2.** An example of LUCI 2 N 3.75 detector linearity map of the linear coefficient. Such maps are available for all linearity and persistence coefficients. The maps give the (zero-point, linear, and quadratic term) coefficient values derived for each pixels, as shown by the examples in Fig. A1.

the ranging behaviour of different pixels, in the figure we show the fits for two pixels at different position on the detector. Each pixel is represented by a four panel figure showing the fits and linearity and persistence correction equations and their coefficients, as described in the figure legend. In the bottom-right-hand panel we show the pixel noise statistics and the fit through it as a function of the duration time of the entire calibration sequence. The latter plot shows that there are no strong trends as a function of time, which might be expected to accumulate due to the persistence.

The zero-point, linear, and quadratic coefficients from the linearity and persistence fits, performed to each pixel of the detector, are stored as six fits image maps. An example of one such map is presented in Fig. A2, which shows the map of the coefficient of the linear term. With this map one can appreciate the large- and small-scale variations of this coefficient. A number of detector features are visible such as groups of bad, hot, or cold pixels and a horizontal stripes pattern from the detector electronics which repeats every 64th column. To appreciate the pixel-to-pixel variation in Fig. B1, we show cuts through the zero-point and linear term maps at two different $x$-pixel locations, 1035 and 1801. The large and small scale trends seen in Fig. A2 are aslo shown in Fig. B1. Positive and negative spikes show hot and cold or bad pixels.

## APPENDIX B: ARGOS PSF PERFORMANCE

To correct the ground layer turbulence, ARGOS uses a constellation of three lasers per telescope evenly situated on a circle with radius of 2 arcmin, which also corrects for the strong anisoplanatism as a function of distance from the NGS. For this particular first science data observation, the NGS was located at the image centre, therefore, it is expected that the effects on the image PSF (elongation, orientation) should be symmetric. We use the measurements from our PSF modelling and photometry described in detail in Section 3.1. The

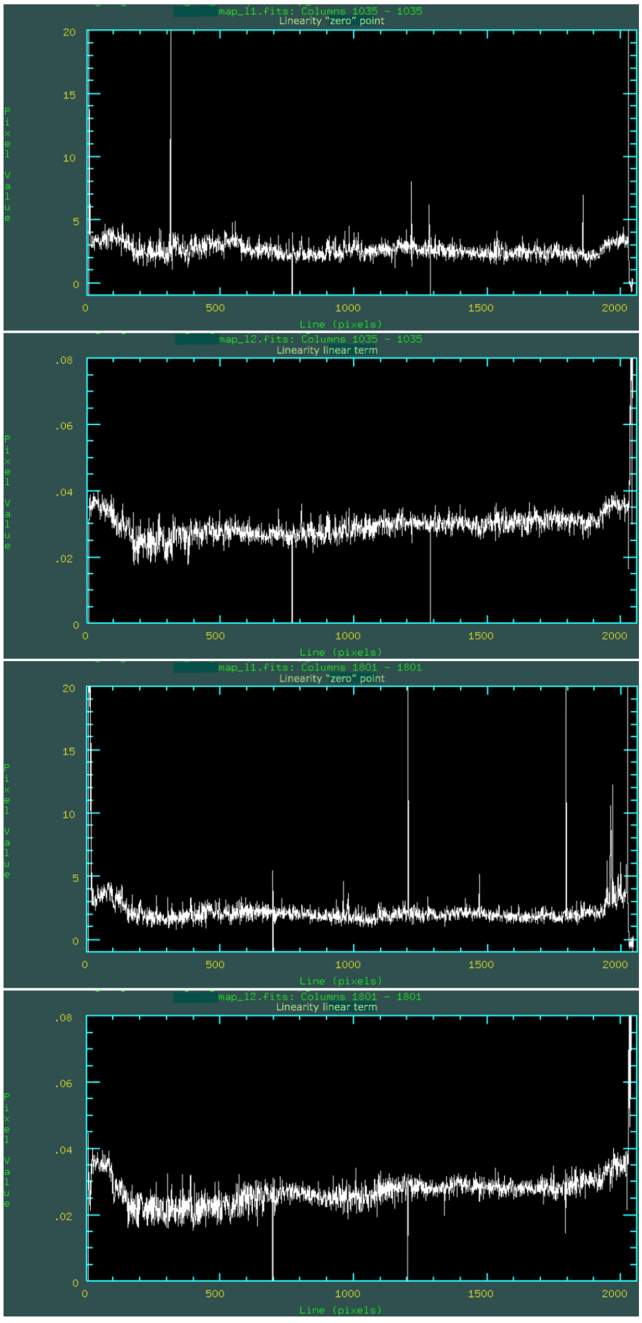


**Figure B1.** An example of linearity zero-point (**left**) and linear coefficient (**right**) values at two different detector X-pixel positions (**top** and **bottom** row) cutting through all detector Y-pixel locations. Cold and hot spikes in the plots indicate cold, hot, or bad pixels.

field of NGC 6384 contains a large number (>100) of foreground Galactic stars. To analyse the angular and radial variation of the ARGOS corrected image PSF, in Fig. B2 we show the FWHM of the PSF ($PSF_{FWHM}$) as a function of the position angle (PA) and the observed *JHKs* filters in the top row and bottom-right panels. With different symbols and colours, we show the three different radial bins, as indicated in the figure legend. The bottom left-hand panel of Fig. B2 illustrates the direction of the PA shown in the other panels and the spatial position of the high-S/N sources on the detector. We fitted the FWHM of the sources within 1 arcmin and between 1 and 2 arcmin distance from the NGS, which are shown as labels for the respective filter in the different panels. Due to the relatively large LUCI 2 field of view for adaptive optics correction, it is expected that some anisoplanatism could still be present as a function of the distance from the NGS to the LGSs, which are situated on a circle of radius 2 arcmin. We see from Fig. B2 that the FWHM fits to sources within 1 arcmin and between 1 and 2 arcmin distance from the NGS differ by up to ∼20 per cent. Sources outside the 2 arcmin radius in the image corners are also seen to be slightly more extended (often with the highest FWHM value), however, due to their relatively low number, we cannot fully quantify the FWHM degradation outside the LGSs circle from this data alone. Overall, for this first commissioning science data and sky quality during the observations, the achieved FWHM correction provided by ARGOS in the NIR is around 0.25–0.3 arcsec, which is also very stable across the detector to within ∼20 per cent.

We examine the elongation and orientation of the $PSF_{FWHM}$ in Fig. B3. The vectors in the figure show the direction of orientation of the PSF for high-S/N sources, which are also colour coded according to their ellipticity. Measured PSF orientation makes sense only for sources with ellipticity larger than about 0.05 (axial ratio $\gtrsim$5 per cent). We can indeed see that most of the sources towards the detector corners, more apparent in *J* band (Fig. B3 left-hand panel), show more radially aligned orientation.

The absolute value of the corrected $PSF_{FWHM}$ is also a function of the natural seeing and sky conditions (e.g. passing high altitude clouds, variable direction, and strength of wind), which obviously can change within the night or from one night to the other. In addition, for such a first commissioning run the ARGOS system performance is not yet optimal and improvement was in progress. To analyse these temporal variations of the image FWHM in Fig. B4, we show the image FWHM for the three filters (*JHKs* top to bottom) as a function of the time when an exposure was taken. We have limited here our analysis only to the data sets which were (partly) used to select the sharpest images for the scientific analysis of the data as described in the main text of this paper. Therefore, we are not showing here the FWHM variation during various phases of the commissioning testing, which is presented in a dedicated ARGOS commissioning paper by Rabien et al. (2018). As it can be seen, the best and most stable image quality (FWHM) was achieved on the night of 2015-05-01 in the *H*-filter (Fig. B4 middle panel). The following night of 2015-05-02 is showing a larger FWHM variation, but improving as a function of time (compare Fig. B4 top and bottom panels). This large-scale FWHM improvement (besides its absolute value due to the difference in the *J* and $K_S$ $PSF_{FWHM}$) is attributed to the improving sky conditions (decreasing wind, improving natural seeing). The variations on small temporal scales are due to broken laser loops, which are either caused by commissioning tests or often by a system pause due to satellite or an airplane passing overhead. The latter two requires lasers shut down and opening the loops. Images taken during that phase often show the natural seeing value in the respective filter. This can be seen in the top panel of Fig. B4 in the *J* band, where loops were broken/paused about three times at around 8.15, 10.2, and 11.4 UT time. Apparently, the night quality was improving and the open loops FWHM value is decreasing. There were few filter changes between *J* and $K_S$ at between 11.5 and 11.62 UT time, but most of the $K_S$-band observations (Fig. B4 bottom) followed the *J*-band data. The combination between improving sky quality and sharper PSF in the $K_S$ provided a nearly diffraction limited sampling of the PSF of $0\farcs24 = 2$ pix, as seen in Fig. B4 bottom panel and from the fits in Fig. B2 bottom-right panel.

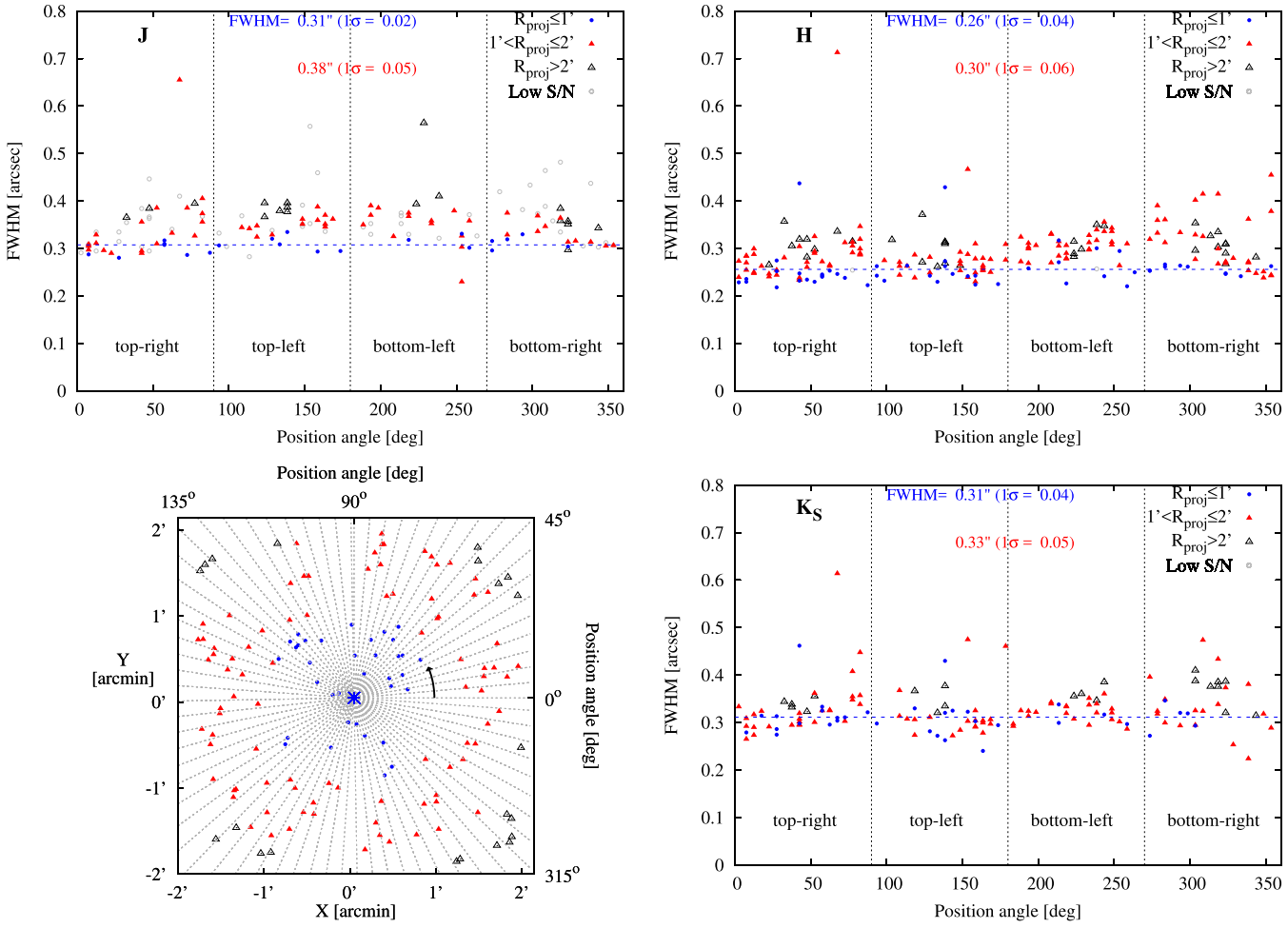


**Figure B2.** ARGOS commissioning data analysis of the angular and radial $PSF_{FWHM}$ variation. The **top two** and **bottom-right** panels show the azimuthal variation of the FWHM in the three filters as labelled. Every symbol is a source in the LUCI 2 image with an S/N > 15, at a given PA and at a radial distance from the NGS (image centre) of $r \leq 1$, $1 \leq r \leq 2$, and $r > 2$ arcmin, as indicated in the figure legend. With a horizontal dashed line is shown the best least-squares fit of the FWHM through the data within $r \leq 1$ arcmin, where its value and $1\sigma$ dispersion are shown with labels, as well as for data within $1 \leq r \leq 2$ arcmin. In the **bottom-left** panel curved arrow starting at 0° shows the PA and its counter clockwise direction of rotation. To guide the eye, with dashed lines are also shown each 5° of PA.

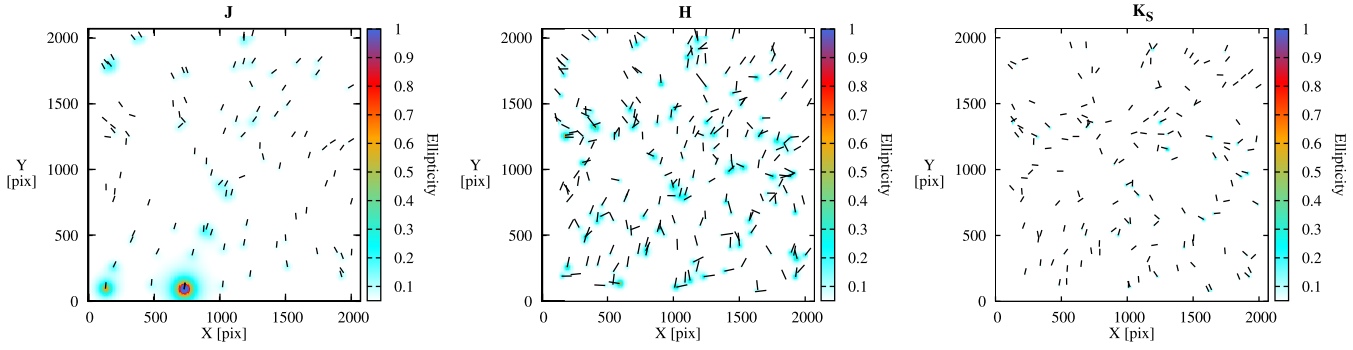


**Figure B3.** PSF ellipticity and orientation analysis. Vectors show the direction of elongation of the PSF for high-S/N sources, which are also colour coded by their PSF ellipticity. The three panels show the data for the three different filters.

Overall, in this section we showed that ARGOS provides LBT with spatially and temporary stable $PSF_{FWHM}$ in the NIR over 4 × 4 arcmin field of view, which is unique for a ground based observatory.

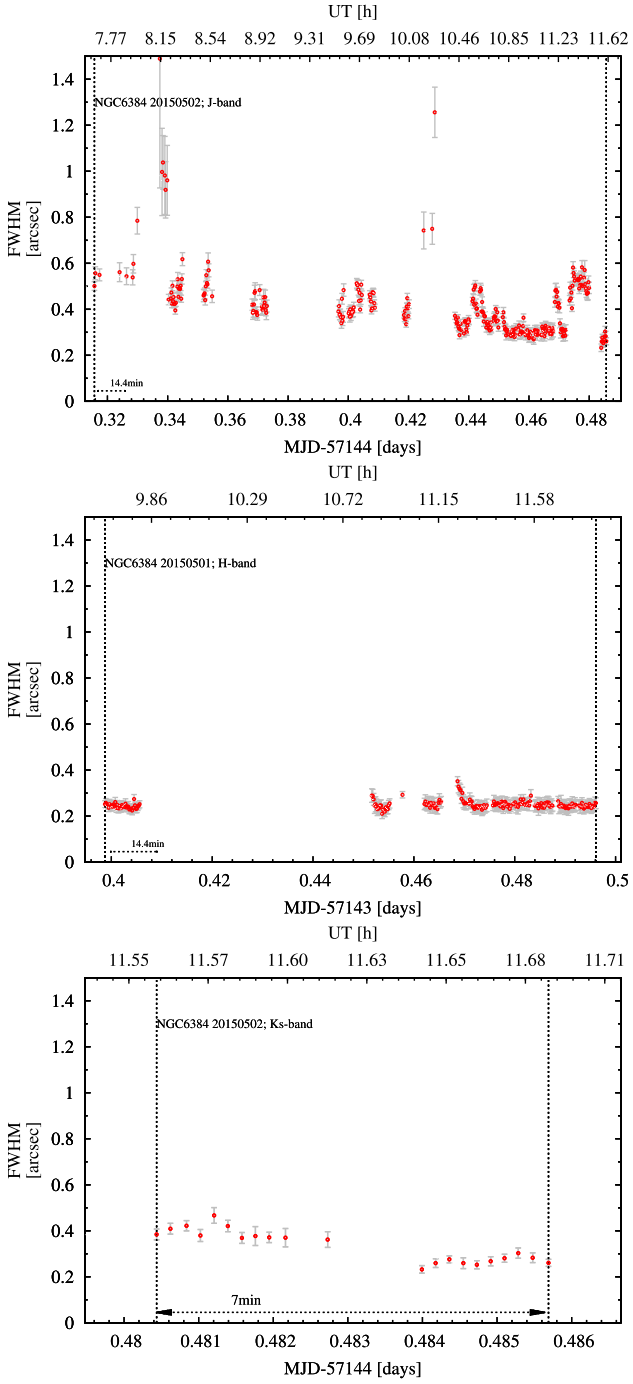


**Figure B4.** ARGOS commissioning data analysis of the temporal $PSF_{FWHM}$ variation. From top to bottom is shown the variation for the three filters, *J*, *H*, and *Ks*, as a function of time [in MJD (days) on the *x*-axis and UT (h) on the *x*2-axis].

## APPENDIX C: MCMC EXPLORATION OF MODEL PARAMETERS AND THEIR UNCERTAINTIES

As described in Section 3.2, we tested a wide variety, and number, of fitting functions that best describe the nuclear cluster and inner regions of NGC 6384. A quick analysis was performed with $\chi^2$ minimization, while the detailed parameter and their uncertainty exploration we conducted with the IMFIT MCMC module. Here we show as an example of this analysis for the $K_S$ band and how we obtained the structural parameters and uncertainties for the NSC and NGC 6384 inner 3.6 × 3.6 kpc (∼36 × 36 arcsec). Fig. C1 shows the corner plot created with the corner module (Foreman-Mackey 2016) of the Astropy channel (Astropy Collaboration 2013; 2018). We explored in total 35 model parameters shared between the five functions – a modified King (Elson 1999; Peng et al. 2010) which for $\alpha = 2$ reduces to the original King (1962); two Sérsic and two generalized elliptical 2D Sérsic and exponential profiles. Their functional forms are given in the IMFIT manual.[12] As it can be seen from Fig. C1, we obtained good convergence and uncertainty estimates for all parameters.

[12] http://www.mpe.mpg.de/∼erwin/resources/imfit/imfit_howto.pdf

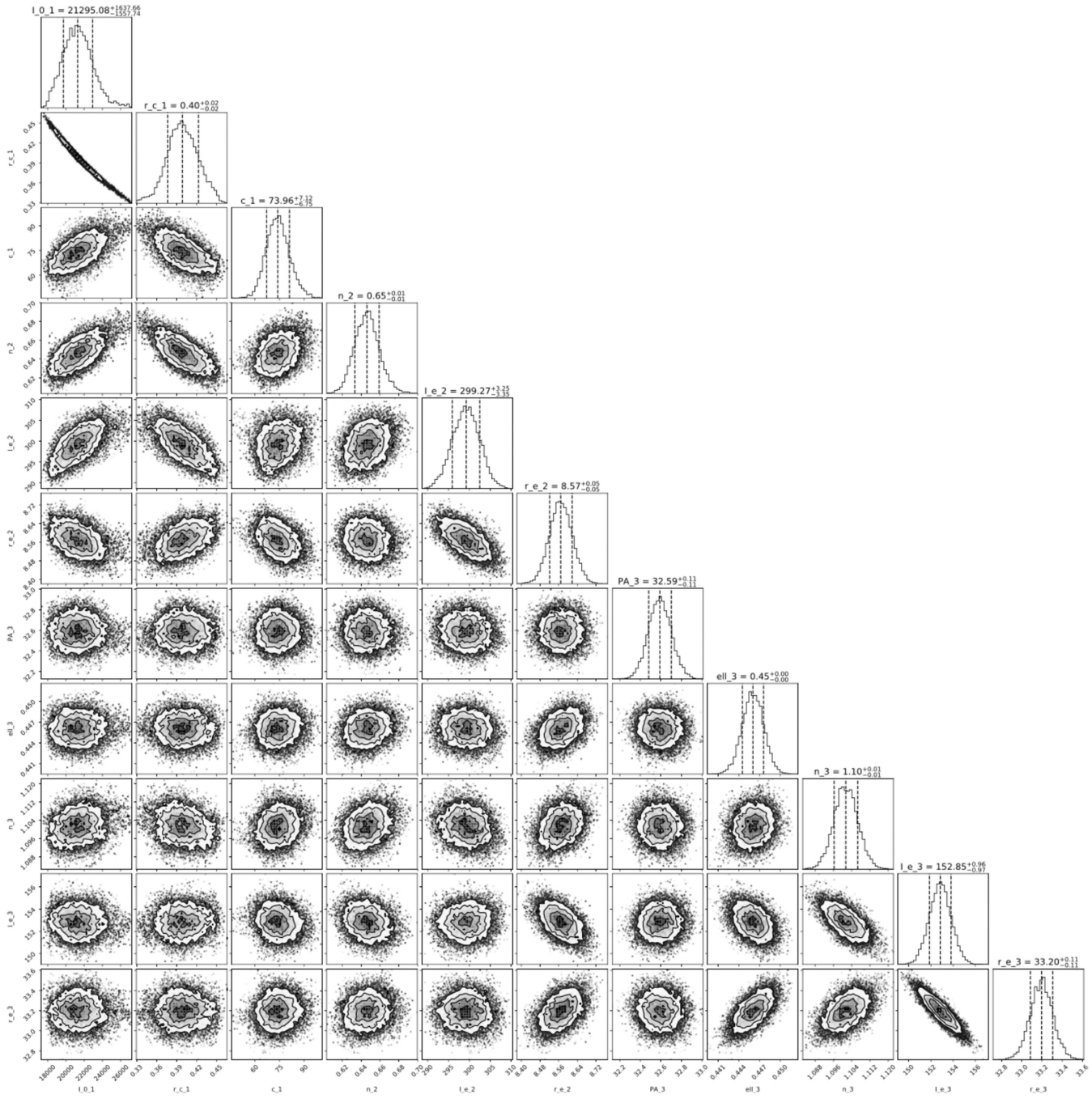


(a)

**Figure C1.** Corner plot of the fitted structural parameters on the $K_S$-band image obtained using the IMFIT MCMC module. The best parameter values and their uncertainties were estimated using the median and their $1\sigma$ values indicated with vertical dashed lines. This plot shows the parameter values for the inner three components: King, inner, and outer Sersić components. Parameter values for the generalized Sersić and exponential profiles.

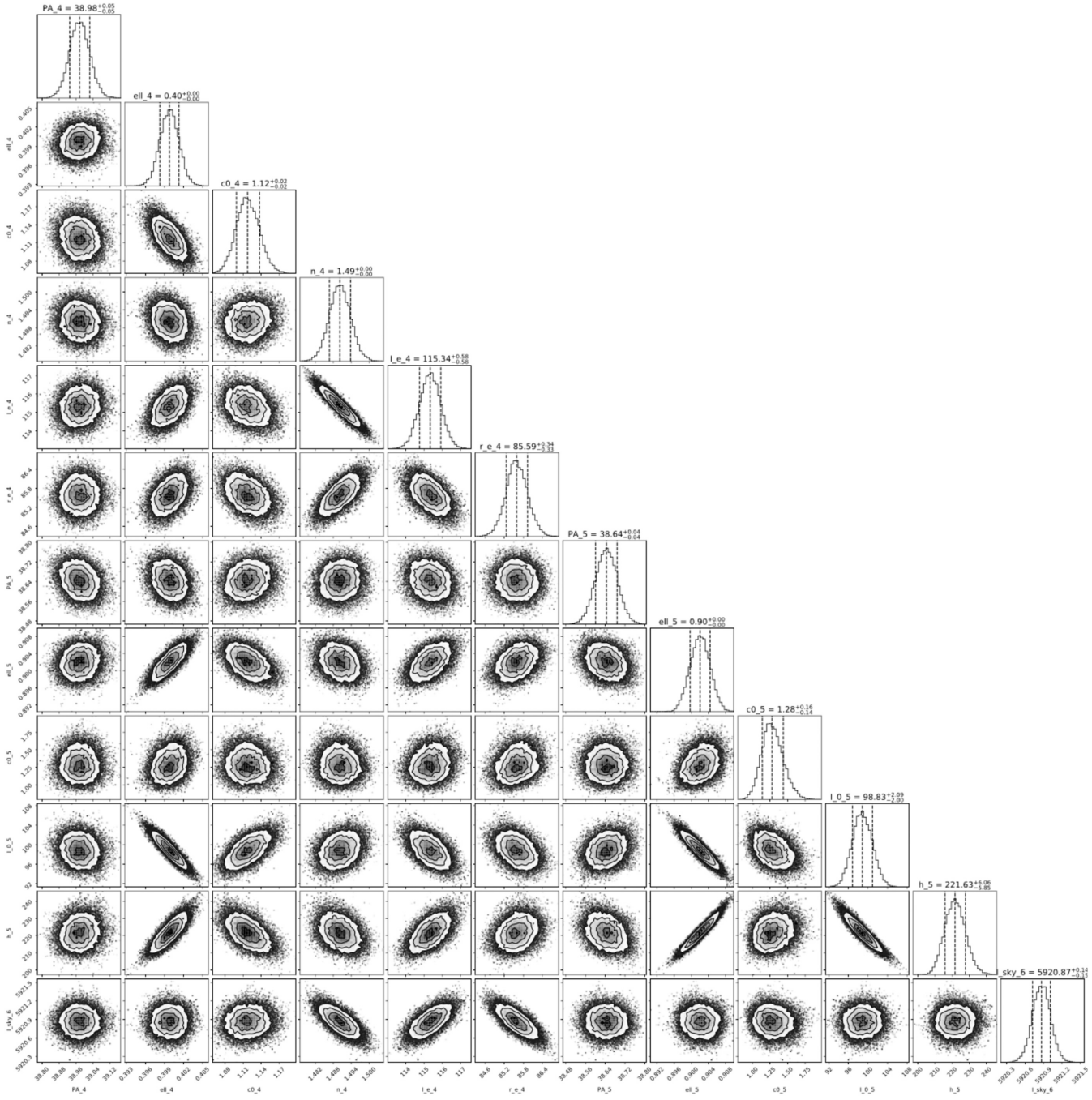


(b)

**Figure C1.** – *continued*

## APPENDIX D: $R_{\rm EFF}$ RELATED TO KING MODEL PARAMETERS

For the original King (1962) model there is no simple analytical connection between the effective radius $r_{\rm eff}$ containing half the mass/light in projection and the parameters of the King profile (core radius, $r_c$, concentration, $C \equiv c = \log_{10}(r_t/r_c)$ and $\alpha$). Here, we derive this connection through direct integration of King (1962) profiles and fitting the resulting values by a polynomial fit. The coefficients of the polynomials have been determined through $\chi^2$ minimization. Our fit between $r_{\rm eff}$, $r_c$, $c$, $\alpha$ was derived for values of $c$ between $0.5 < c < 3.0$ and $\alpha$ between $0.25 < \alpha < 5.0$. This resulted in the following fit:

$$\log_{10}(r_{\rm eff}/r_c) = c_1 + c_2 \times \alpha + c_3 \times \alpha^2 + c_4 \times \alpha^3, \quad \text{(D1)}$$

where the coefficients $c_1, c_2, c_3, c_4$ are given by

$$\begin{bmatrix} c_1 \\ c_2 \\ c_3 \\ c_4 \end{bmatrix} = \begin{bmatrix} -0.13150 & 0.74000 & -0.10900 & 0.01569 \\ -0.13980 & -0.05897 & 0.03980 & -0.00558 \\ 0.02390 & 0.00112 & -0.01689 & 0.00307 \\ -0.00198 & 0.00080 & 0.00166 & -0.00035 \end{bmatrix} \times \begin{bmatrix} 1 \\ c \\ c^2 \\ c^3 \end{bmatrix}.$$

We used this relation to calculate the NSC $r_{\rm eff}$ given in Table 1. These relations are good to within a per cent. Often, fitting can report the measured FWHM, therefore, similarly, we also obtained the relation between the effective radius and the FWHM as follows:

$$\log_{10}(r_{\rm eff}/r_{\rm FWHM}) = c_1 + c_2 \times \alpha + c_3 \times \alpha^2 + c_4 \times \alpha^3, \quad \text{(D2)}$$

with the following values for the coefficients $c_1, c_2, c_3, c_4$:

$$\begin{bmatrix} c_1 \\ c_2 \\ c_3 \\ c_4 \end{bmatrix} = \begin{bmatrix} -0.20070 & 0.85499 & -0.16590 & 0.02455 \\ 0.05510 & -0.40780 & 0.22090 & -0.03462 \\ 0.00264 & 0.07583 & -0.06395 & 0.01131 \\ -0.00143 & -0.00456 & 0.00559 & -0.00109 \end{bmatrix} \times \begin{bmatrix} 1 \\ c \\ c^2 \\ c^3 \end{bmatrix}.$$

An illustration of these relations we show in Fig. D1 for few fixed concentration indexes. As it can be seen from the figure, the achieved precision is much less than 1 per cent.

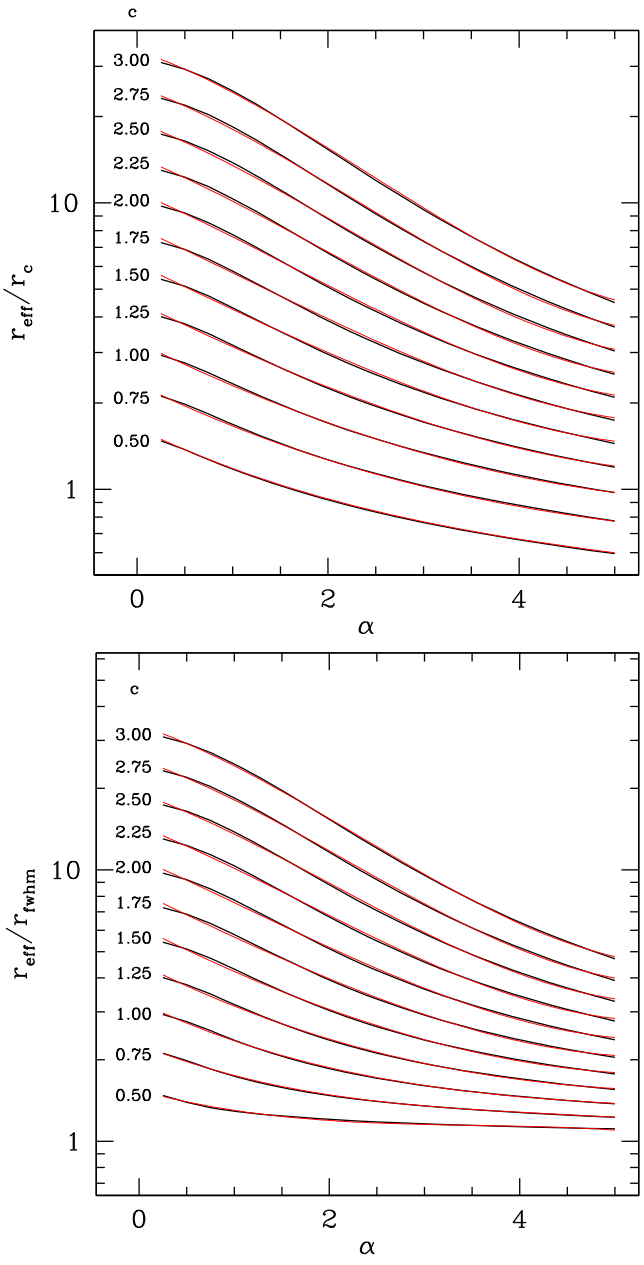


**Figure D1.** Illustration of the relation between $r_{\rm eff}$ and $r_c$ (left) and between $r_{\rm fwhm}$ and $r_c$ (right) for King (1962) models for few discrete values of the concentration index $c$. Black curves show the actual values determined by integration of the King profiles while the red curves are out fit according to equations D2 and D1.

This paper has been typeset from a TEX/LATEX file prepared by the author.